University of New Mexico
UNM Digital Repository

Electrical and Computer Engineering ETDs
Engineering ETDs

1-29-2009

Development of indium arsenide quantum dot solar cells for high conversion efficiency

Mohamed El-Emawy

Follow this and additional works at: https://digitalrepository.unm.edu/ece_etds

Recommended Citation

El-Emawy, Mohamed. "Development of indium arsenide quantum dot solar cells for high conversion efficiency." (2009). https://digitalrepository.unm.edu/ece_etds/73

This Thesis is brought to you for free and open access by the Engineering ETDs at UNM Digital Repository. It has been accepted for inclusion in Electrical and Computer Engineering ETDs by an authorized administrator of UNM Digital Repository. For more information, please contact disc@unm.edu.

Mohamed Abdel Rahman El-Emawy

Candidate

Department of Electrical and Computer Engineering

Department

This thesis is approved, and it is acceptable in quality and form for publication on microfilm:

Approved by the Thesis Committee:

Prof. Luke F. Lester , Chairperson

Dr. Andreas Stintz

Dr. Frederic Grillot

Dr. Ganesh Balakrishnan

Accepted:

Dean, Graduate School

Date

DEVELOPMENT OF INDIUM ARSENIDE QUANTUM DOT SOLAR CELLS FOR HIGH CONVERSION EFFICIENCY

BY

MOHAMED ABDEL RAHMAN EL-EMAWY

B.S., ELECTRICAL ENGINEERING, UNIVERSITY OF NEW MEXICO, 2006

THESIS

Submitted in Partial Fulfillment of the
Requirements for the Degree of

Master of Science
Electrical Engineering

The University of New Mexico
Albuquerque, New Mexico

December, 2008

©2008, Mohamed Abdel Rahman El-Emawy

DEDICATION

To My Parents

ACKNOWLEDGMENTS

I would like to express my thanks to my advisor Professor Luke F. Lester for his guidance and assistance over the course of my research at the Center for High Technology Materials (CHTM). I have learned a great deal in the area of optoelectronics over the past couple of years through his help and motivation.

I would like also to thank all of my colleagues, Furqan Chiragh and Mike Pochet for reviewing my thesis and providing me with valuable comments. I thank Aaron Moscho for teaching me how to process solar cells and using the clean room tools. My thanks are due to Nader Naderi, Chang-Yi Lin, Tron Nilsen, Therese Saiz, William Zortman, Tingyi Gu, Jeremy Wright, and Dr. Yongchun Xin for their assistance and input in this thesis.

I would like to thank the rest of my committee members, Dr. Andreas Stintz, Dr. Frederic Grillot, and Dr. Ganesh Balakrishnan, for their valuable recommendations and important suggestions.

Finally, I would like to express my thanks and love to my family for their continuous support and encouragement.

Thank You All.

DEVELOPMENT OF INDIUM ARSENIDE QUANTUM DOT SOLAR CELLS FOR HIGH CONVERSION EFFICIENCY

BY

MOHAMED ABDEL RAHMAN EL-EMAWY

ABSTRACT OF THESIS

Submitted in Partial Fulfillment of the
Requirements for the Degree of

Master of Science
Electrical Engineering

The University of New Mexico
Albuquerque, New Mexico

December, 2008

DEVELOPMENT OF INDIUM ARSENIDE QUANTUM DOT SOLAR CELLS FOR HIGH CONVERSION EFFICIENCY

by

Mohamed Abdel Rahman El-Emawy

B.S., Electrical Engineering, University of New Mexico, 2006

M.S., Electrical Engineering, University of New Mexico, 2008

ABSTRACT

Sunlight is the largest energy source available on earth. Under clear conditions there is approximately 1,000 watts per directly incident square meter, which reaches the earth everyday. Solar cells are devices that can be used to collect such abundant form of energy and convert it into electrical energy for daily consumption. Therefore, it is important to research this subject in order to obtain high efficiency solar cells.

In this thesis InAs quantum dot (QD) solar cells are studied and investigated. The theory of using QDs as an intermediate band in GaAs-based solar cells is introduced. Three samples are grown for investigation, an MBE grown GaAs control cell, an MBE grown six-stack InAs QD solar cell, and an MOCVD grown three-stack InAs QD solar cell. Inductively coupled plasma (ICP) etch without Si_3N_4 sidewall passivation and wet etch using Si_3N_4 sidewall passivation are implemented to process the solar cells, to study the effects of processing on the device performance.

Spectral response measurements show photocurrents above the GaAs wavelength indicating the contribution from the InAs QDs in the structure. From the I-V measurements, efficiencies for the GaAs control cell, MBE six-stack InAs QD, and MOCVD three-stack InAs QD solar cells are 8.95%, 6.55%, and 1.33%, respectively. Wet etching with Si_3N_4 sidewall passivation shows slightly higher efficiency for the MBE six-stack sample.

Sizing effects of the 5x5mm, 3x3mm, and 2x2mm for the MBE grown six-stack InAs QD solar cells show that the device efficiency and open circuit voltage do not change with size. The 2x2mm solar cell exhibits improvement in the ideality factor, shunt resistance, and saturation current.

Some future work suggestions are given to increase the InAs QD solar cells such as multilayer structures with embedded InAs QD using different processing techniques.

TABLE OF CONTENTS

DEDICATION ... iv

ACKNOWLEDGMENTS ... v

ABSTRACT ... vii

LIST OF FIGURES ... xii

LIST OF TABLES ... xvi

CHAPTER 1 - Solar Cell Theory of Operations ... 1

1.1 Introduction ... 1

1.2 Solar Cell Basic Principles ... 3

1.2.1 Solar cell I-V characteristics ... 3

1.2.2 Non-ideal pn junction ... 5

1.2.3 Open circuit voltage, V_{oc}, and short-circuit current, I_{sc} ... 6

1.2.4 Maximum power delivered to the load ... 6

1.2.5 Solar cell fill factor ... 8

1.2.6 Solar cell conversion efficiency ... 8

1.2.7 Ideality factor and saturation current ... 8

1.2.8 Series and shunt resistances ... 9

1.2.9 Solar cell spectral response ... 9

1.2.10 External quantum efficiency ... 11

1.3 Materials and Design Considerations ... 11

1.4 Types of Solar Cells ... 12

1.4.1 Homojunction solar cells ... 12

1.4.2 Heterojunction solar cells ... 13

1.4.3 Multijuction solar cells 14
1.5 Organization of Thesis 15
CHAPTER 2 - Research Review 16
2.1 Multijunction Solar Cells 16
2.2 Intermediate Band Solar Cells (IBSC) 17
2.3 Density of States 19
2.4 Quantum Wells as Intermediate Band for Solar Cells 21
2.5 Quantum Wires as Intermediate Band for Solar Cells 22
2.6 Quantum Dots as Intermediate Band for Solar Cells 23
2.7 Why QD IBSC? 25
CHAPTER 3 - Solar Cells Material Structure and Characterization 26
3.1 The PIN Diode 26
3.2 Energy Band Diagram of QD-based Solar Cells 27
3.3 Solar Cells Structures 28
3.4 Molecular Beam Epitaxy (MBE) Growth of Solar cells 31
3.5 Growth Characterization of MBE-Grown QDs 31
3.6 Metal Organic Chemical Vapor Deposition (MOCVD) Growth of Solar Cells33
3.7 Growth Characterization of MOCVD-Grown QDs 34
CHAPTER 4 - Solar Cells Processing and Fabrication 37
4.1 Sample Preparation Fabrication Steps 38
4.2 Inductively Coupled Plasma (ICP) Etching without Sidewall Passivation 38
4.3 Wet Etched Mesa with Sidewall Passivation 44
CHAPTER 5 - InAs QD Solar Cells Characterization 47

5.1 Device Characterization ... 47
5.1.1 I-V Experimental Setup ... 47
5.1.2 Spectral Response Experimental Setup ... 49
5.2 Characterization of ICP Etched-Mesa Solar Cells Fabricated without Silicon Nitride Sidewall Passivation ... 50
5.2.1 I-V Measurements of the ICP etched solar cells without silicon nitride sidewall passivation ... 50
5.2.2 Spectral response measurements of the ICP etched solar cells fabricated without silicon nitride sidewall passivation ... 55
5.3 Characterization of the Wet Etched Mesa Solar Cells Fabricated with Silicon Nitride Sidewall Passivation ... 57
5.3.1 I-V measurements of the wet etched solar cells fabricated with silicon nitride sidewall passivation ... 57
5.3.2 Spectral Response Measurements of the Wet Etched Solar Cells Fabricated with Silicon Nitride Sidewall Passivation ... 60
5.4 Scaling Effects of Six-Stack InAs QD Solar Cells ... 61
CHAPTER 6 - Conclusion and Future Work ... 68
REFRENCES ... 71

LIST OF FIGURES

Figure 1.1 Solar spectral irradiance. [2] 2

Figure 1.2 A pn junction solar cell with the resistive load. 3

Figure 1.3 Non-ideal solar cell equivalent circuit. 5

Figure 1.4 (a) Solar cell schematic. (b) Typical I-V characteristics of the solar cell with the maximum power rectangular determined by V_m and I_m. [5] 7

Figure 1.5 Series resistance and shunt resistance from IV curve. [6] 9

Figure 1.6 One-dimensional model of a junction solar cell. 10

Figure 1.7 GaAs homojunction solar cell. 13

Figure 1.8 Lattice constant and bandgap of common semiconductor materials. [11] 14

Figure 1.9 (a) Multijunction solar cell bandgap arrangement. (b)A structure of multijunction solar cell. [16] 15

Figure 2.1 I-V Characteristic for metamorphic $Ga_{0.44}In_{0.56}P/Ga_{0.92}In_{0.08}As/Ge$ and lattice-matched $Ga_{0.50}In_{0.50}P/Ga_{0.99}In_{0.01}As/Ge$ three-junction terrestrial solar cells. [17] 16

Figure 2.2 Schematic representation for Intermediate band absorption employed in solar cells structure to increase their conversion efficiency. [18] 17

Figure 2.3 IBSC calculated theoretical efficiencies as a function of intermediate bandgap (IB). The single junction cells, and tandem cells are shown compared to the IBSC model. [1] 18

Figure 2.4 Semiconductor bulk, quantum well, quantum wire, and quantum dot structures density of states. [21] 20

Figure 2.5 QW pin solar cell schematic operation. [24] 22

Figure 2.6 Carrier excitation demonstrated (A) without and (B) with carrier multiplication. [27] 24

Figure 3.1 Schematic representation of the pin solar cell structure. 27

Figure 3.2 Energy band diagram for InAs/GaAs QD solar cell heterostructure. 28

Figure 3.3 Samples structures of (a) MBE grown GaAs control cell, run2609 (b) MBE grown 6-stack InAs QD cell, run2611. 29

Figure 3.4 Samples structures of MOCVD grown 3-stack InAs QD cell. 30

Figure 3.5 Schematic representation of a typical MBE chamber with five effusion cells and RHEED gun. [35] 31

Figure 3.6 Atomic force microscope images of InAs QDs grown on $In_{0.15}Ga_{0.85}As$ buffer layers at 470° C. The scan size is 500 nm x 500 nm. [36] 32

Figure 3.7 Photoluminescence measurement for sample run2609 (control cell) and sample run2611 (6-stack QD cell). 33

Figure 3.8 Schematic representation for a typical MOCVD chamber where source materials with carrier gas are mixed in the main manifold before the reaction takes place in the chamber. [37] 34

Figure 3.9 Atomic force microscope images of InAs QDs grown on $In_{0.15}Ga_{0.85}As$ buffer layers at 500° C. The scan size is 1 μm x1 μm. [38] 35

Figure 3.10 Room-temperature PL spectrum of capped InAs QDs grown on $In_{0.15}Ga_{0.85}As$ at 500° C. The cap layers, grown at 500 °C, are 45 Å of $In_{0.15}Ga_{0.85}As$ and 330 Å of GaAs. 36

Figure 4.1 Schematic representation of the processing steps using inductively coupled plasma (ICP) etching without sidewall passivation. 39

Figure 4.2 Photograph of mask 1 for the solar cell patterns. Three different areas are shown 5x5 mm, 3x3 mm, and 2x2 mm. Metallization of probing pad, bus, and fingers are also shown for the three different solar cells. 40

Figure 4.3 A photograph of mask #2 used to remove antireflection coating from the contact pad and the solar cell boundary. 42

Figure 4.4 A photograph of mask #3 used to identify the final mesa solar cell structure. 43

Figure 4.5 (a) Processed quarter wafer (b) Cross-sectional view of mesa structure......... 44

Figure 4.6 Schematic representation for the processing steps using wet etching with sidewall passivated mesa structure. 45

Figure 4.7 Cross-sectional view of wet etched mesa structure. 46

Figure 5.1 A schematic representation of the setup used to measure the I-V characteristics of solar cells. 48

Figure 5.2 A schematic representation of the setup used to measure the spectral response characteristics for solar cells. 49

Figure 5.3 I-V characteristics for the 5x5mm ICP etched and unpassivated mesa solar cells. Control (red), 6-stack InAs QD (blue) and 3-stack InAs QD (green) solar cells processed under the same conditions. 51

Figure 5.4 Equivalent circuit for resistance mechanisms involved in a solar cell. 55

Figure 5.5 The Spectral response for the 5x5mm control (red), 6-stack InAs QD(blue) and 3-stack InAs QD (green) solar cells fabricated by ICP etching and without sidewall passivation.. 56

Figure 5.6 The I-V characteristics for the 5x5mm GaAs control cell (red) and the 6-stack InAs QD(blue) solar cells fabricated by wet etching and passivated by silicon nitride. .. 58

Figure 5.7 The Spectral response for the 5x5mm control (red) and 6-stack InAs QD (blue) solar cells fabricated by wet etching and passivated by silicon nitride. 60

Figure 5.8 The I-V characteristics for the5x5mm (red), 3x3 mm (blue), and 2x2 mm (green) InAs six-stack QD solar cells. (a) ICP etched without silicon nitride passivation, (b) Wet etched with silicon nitride passivation. Both techniques show an obvious increase in the I_{sc}. 62

Figure 5.9 Six-stack InAs QD solar cell short circuit current versus solar cell area. 65

Figure 5.10 A simple model for the series resistance components when the solar cell device is scaled. 65

Figure 5.11 Solar cell illustration showing the finger length and finger gap. 66

LIST OF TABLES

Table 5.1 Data summary for the 5x5mm control, 6-stack InAs QD and 3-stack InAs QD solar cells fabricated by ICP etching and without sidewall passivation. 53

Table 5.2 Summary for the MBE grown 5x5mm control and the 6-stack InAs QD solar cells fabricated by wet etching and passivated by silicon nitride. 59

Table 5.3 Summary for the 5x5mm, 3x3mm, and 2x2mm InAs six-stack QD solar cells. (a) ICP etched without silicon nitride passivation, (b) Wet etched with silicon nitride passivation.. 64

Table 5.4 Finger length and gap for the 5x5mm, 3x3mm, and 2x2m solar cells. 66

Table 5.5 Sheet resistance values for the two six-stack InAs QD 5x5mm, 3x3mm, and 2x2m solar cells. 67

CHAPTER 1 - Solar Cell Theory of Operations

Energy sources are crucial for the development of human societies. Everyday different forms of energy are being consumed to produce electricity, which is a necessity of everyday life. Sunlight is considered the largest energy source available on earth. There is approximately 1,000 watts per directly incident square meter, which reaches the earth everyday in clear conditions. Therefore, the main problem with today's high demand for energy could be solved if the incident light on the earth were harvested efficiently. This can be achieved by utilizing solar cells, which collect the incident sunlight and convert it to current. Unfortunately, much work is needed to improve the solar cell efficiency, to absorb as much as possible of the abundant incident light. In this thesis, InAs quantum dot (QD) solar cells are introduced and examined. The main reason of interest behind the QD solar cell is that it has been shown theoretically that the calculated efficiency can reach as high as 63% [1]. If realized, this percentage will set an all time record for solar cell efficiency. Therefore, it is important to introduce the basic principles of solar cell operation, in order to understand its basic functions.

1.1 Introduction

Solar cells are made of different semiconductor materials to convert solar energy into electrical energy. The energy obtained from the solar cells is a renewable source and does not have any adverse effect to the environment. Therefore, solar cells are expected to replace many other sources with less operational cost and minimum maintenance. A

solar cell is a pn junction device with no biasing that delivers photocurrent to the external load.

The sun's energy is electromagnetic radiation with wavelengths ranging from roughly 0.2 – 3.0 micrometers. The sun's radiation reaching the earth is reduced by scattering and absorption in the atmospheric layer. Figure 1.1 shows the solar spectral irradiance where air mass zero (AM0) represents the solar spectrum outside the earth's atmosphere and air mass one (AM1) is the solar spectrum at the earth's surface at the equator at sea level at noon. Depending on the angle of incidence at which the radiation strikes the surface, the intensity can vary between 500 W/m^2 to 1000 W/m^2.

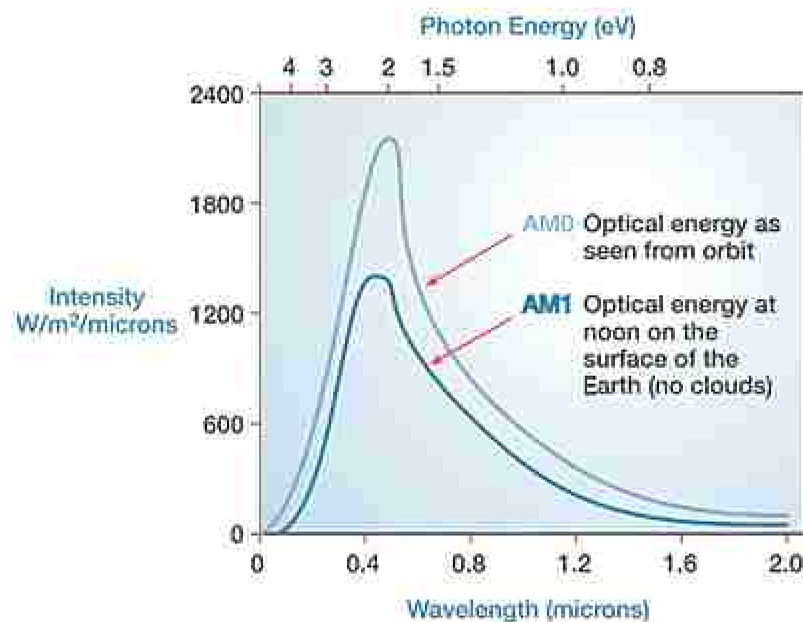

Figure 1.1 Solar spectral irradiance. [2]

The efficiency of a solar cell depends on the materials it is comprised of, its design, and the sun's radiation characteristics at the location of operation. There are different designs regarding solar cell structures, such as homojunction, heterojunction and

multijunction devices. These design structures are implemented to achieve high efficiency solar cells [3].

1.2 Solar Cell Basic Principles

This section will cover the I-V characteristics of the ideal and non-ideal pn junction solar cell assuming uniform generation of electron-hole pairs. From the I-V characteristics, the solar cell efficiency and fill factor equations can be deduced.

1.2.1 Solar cell I-V characteristics

Consider the ideal pn junction shown in Figure 1.2 with the external resistive load, *R*. With no bias applied to the junction, an electric field exists in the depletion region. Under illumination electron-hole pairs will be generated and will be swept out producing a photocurrent I_{ph} in the reverse bias direction as shown in the figure. The photocurrent produces a voltage drop across the load which forward biases the pn junction. Therefore, a forward-bias current I_F is produced. The net current is given by [4]:

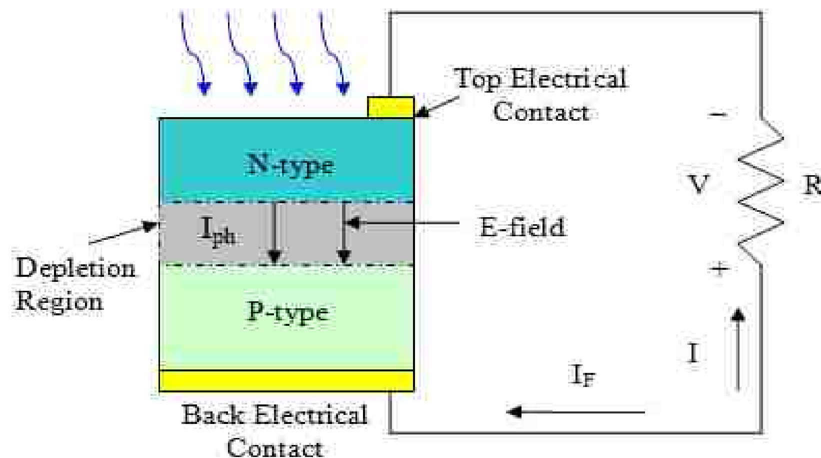

Figure 1.2 A pn junction solar cell with the resistive load.

$$I = I_F - I_{ph} = I_s\left[\exp\left(\frac{qV}{n \cdot kT}\right) - 1\right] - I_{ph} \qquad (1.1)$$

Where:

$$I_{ph} = qAG(L_h + L_e) \qquad (1.2)$$

and

$$I_s = qA\left(\frac{L_h}{\tau_h} p_{no} + \frac{L_e}{\tau_e} n_{po}\right) = qAn_i^2\left(\frac{L_h}{\tau_h N_a} + \frac{L_e}{\tau_e N_d}\right) \qquad (1.3)$$

By substituting equations 1.2 and 1.3 into equation 1.1 we obtain the general I-V relationship for a solar cell, which is:

$$I = qAn_i^2\left(\frac{L_h}{\tau_h N_a} + \frac{L_e}{\tau_e N_d}\right)\left(\exp\left(\frac{qV}{n \cdot kT}\right) - 1\right) - qAG(L_h + L_e) \qquad (1.4)$$

Where:

I_s	reverse saturation current
n	ideality factor
A	area of the diode
G	electron-hole pair generation rate ($cm^{-3}.sec^{-1}$)
L_h (L_e)	hole (electron) diffusion length in the n-side (p-side)
τ_h (τ_e)	minority hole (electron) life time in the n-side (p-side)
n_{po} (p_{no})	equilibrium minority carrier concentration of electrons (holes) in the p-type (n-type) semiconductor
n_i	intrinsic concentration
N_d (N_a)	donor and acceptor concentrations in the material

1.2.2 Non-ideal pn junction

In the non-ideal pn junction case, both the series resistance R_s and shunt resistance R_p must be considered. The series resistance is the result of the electrons' paths in the n-layer surface to the top metal contact. While, the shunt resistance is the resistance through the device which prevents photogenerated carries to flow. It is desired to have the R_s very small (~0) and R_p to be very large (~∞). Both parameters can greatly affect the solar cell performance, i.e. efficiency. Figure 1.3 shows the equivalent circuit for the non-ideal solar cell.

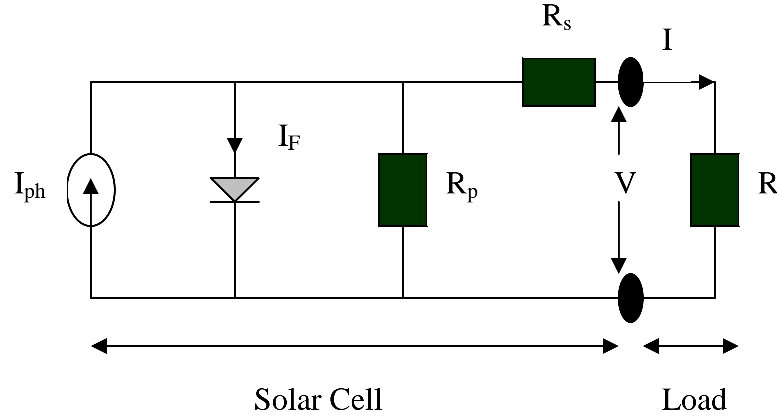

Figure 1.3 Non-ideal solar cell equivalent circuit.

Therefore, equation 1.1 can be rewritten as:

$$I = I_s\left[\exp\left(\frac{q(V + I \cdot R_s)}{n \cdot kT}\right) - 1\right] + \left(\frac{V + I \cdot R_S}{R_P}\right) - I_{ph} \quad (1.5)$$

By substituting equations 1.2 and 1.3 into equation 1.5 we obtain the general I-V relationship for a solar cell, which is:

$$I = qAn_i^2\left(\frac{L_h}{\tau_h N_a} + \frac{L_e}{\tau_e N_d}\right)\left[\exp\left(\frac{q(V + I \cdot R_s)}{n \cdot kT}\right) - 1\right] + \left(\frac{V + I \cdot R_S}{R_P}\right) - qAG(L_h + L_e) \quad (1.6)$$

1.2.3 Open circuit voltage, V_{oc}, and short-circuit current, I_{sc}

Open circuit voltage occurs when the load resistor is disconnected, which means, the net current is zero. Therefore, from equation 1.4 we obtain: Assuming that R_p is infinite, so all the current flows thru the diode.

$$V_{oc} = \frac{kT}{q}\ln\left(\frac{G(L_h + L_e)}{n_i^2\left(\frac{L_h}{\tau_h N_a} + \frac{L_e}{\tau_e N_d}\right)} + 1\right) = V_t \ln\left(\frac{I_{ph}}{I_s} + 1\right) \quad (1.7)$$

Short circuit current occurs when the load is shorted, meaning the drop voltage *V* is zero, and therefore from equation 1.4 we obtain:

$$I_{sc} = I_{ph} = qAG(L_h + L_e) \quad (1.8)$$

Equations 1.7 and 1.8 suggest that V_{oc} and I_{sc} increase indefinitely with the generation rate, *G*. However, as *G* increases the number of electron-hole pairs increase, which decreases $\tau_{h.e}$, therefore I_{sc} increases with *G* while V_{oc} saturates and its maximum value is limited by V_{bi}, which is the built in voltage of the diode.

1.2.4 Maximum power delivered to the load

Assuming the ideality factor $n = 1$, the power delivered to the load is given by:

$$P = IV = qAG(L_h + L_e)V - qAn_i^2\left(\frac{L_h}{\tau_h N_a} + \frac{L_e}{\tau_e N_d}\right)\left(\exp\left(\frac{qV}{kT}\right) - 1\right)V \quad (1.9)$$

Maximum power is obtained by setting the derivative with respect to voltage of equation 1.9 equal to zero, yielding:

$$\left(1+\frac{V_m}{V_t}\right)\exp\left(\frac{qV_m}{kT}\right)=\left(1+\frac{G(L_h+L_e)}{n_i^2\left(\frac{L_h}{\tau_h N_a}+\frac{L_e}{\tau_e N_d}\right)}\right)=\left(1+\frac{I_{ph}}{I_s}\right) \quad (1.10)$$

From equation 1.10, the maximum voltage and the maximum current are expressed as:

$$V_m=\frac{kT}{q}\ln\left(\frac{1+\frac{I_{ph}}{I_s}}{1+\frac{qV_m}{kT}}\right)=V_{oc}-\frac{kT}{q}\ln\left(1+\frac{qV_m}{kT}\right) \quad (1.11)$$

$$I_m=I_s\frac{qV_m}{kT}\exp\left(\frac{qV_m}{kT}\right)\cong I_{ph}\left(1-\frac{1}{\frac{qV_m}{kT}}\right) \quad (1.12)$$

From equations 1.11 and 1.12 the maximum power delivered to the load, assuming $V \sim V_{oc}$, is:

$$P_m=V_mI_m=I_{ph}\left[V_{oc}-\frac{kT}{q}\ln\left(1+\frac{qV_m}{kT}\right)-\frac{kT}{q}\right] \quad (1.13)$$

Figure 1.4 shows the I-V characteristics of the solar cell with the maximum power rectangular where I_m is the current when $V = V_m$.

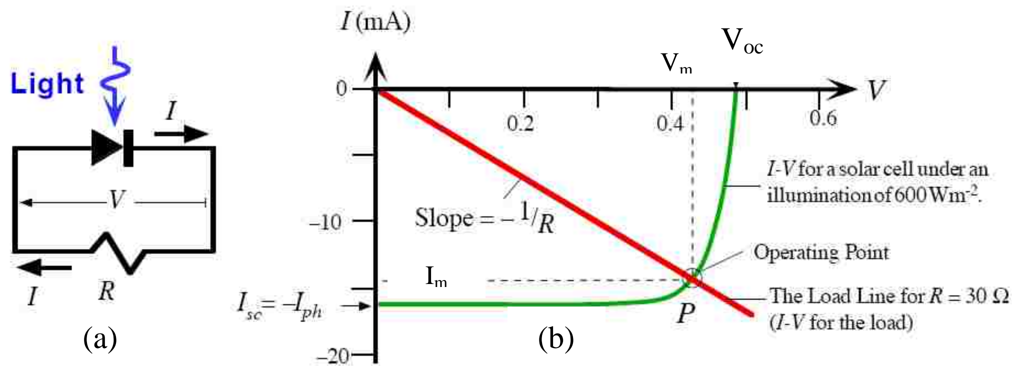

Figure 1.4 (a) Solar cell schematic. (b) Typical I-V characteristics of the solar cell with the maximum power rectangular determined by V_m and I_m. [5]

1.2.5 Solar cell fill factor

The solar cell Fill Factor (FF) is defined as the ratio of the maximum power to the maximum possible current and voltage. The FF is given by:

$$FF = \frac{I_{\max} V_{\max}}{I_{sc} V_{oc}} \qquad (1.14)$$

1.2.6 Solar cell conversion efficiency

The conversion efficiency of a solar cell is defined as the ratio between the maximum output power to the incident optical power, which is:

$$\eta = \frac{P_m}{P_{inc}} x100 = \frac{I_m V_m}{P_{inc}} x100 = \frac{V_m^2 I_s \left(\frac{q}{kT}\right) \exp\left(\frac{qV_m}{kT}\right)}{p_{inc}} x100 \qquad (1.15)$$

1.2.7 Ideality factor and saturation current

By measuring the I-V characteristics of solar cells under dark conditions one can evaluate the ideality factor and saturation current. Under these conditions, the net current equation does not have a photocurrent component. Therefore, the net current can be expressed as shown in equation 1.16. Notice here that the -1 term is omitted since V is much greater than $\frac{n.kT}{q}$.

$$I = (I_{ph} = 0) - I_F = I_s \left[\exp\left(\frac{qV}{n \cdot kT} \right) \right] \qquad (1.16)$$

By taking the natural logarithm of both sides and rearranging terms a new expression can be deduced. This new expression can be used to solve for the ideality factor and saturation current.

$$\ln(\frac{I}{I_s}) = \frac{qV}{n \cdot kT} \Rightarrow \ln(I) = \frac{qV}{n \cdot kT} - \ln(I_s) \qquad (1.17)$$

1.2.8 Series and shunt resistances

There are two main resistance parameters that must be taken into account for solar cell measurements, the series resistance, R_s, and the shunt resistance, R_p. In the ideal solar cell case, R_s is approximately zero and R_p is approximately infinity. In the non-ideal case, both parameters must be evaluated by the IV characteristic curve [6]. Figure 1.5 demonstrates the method to obtain the resistance values for R_s and R_p from the I-V characteristics.

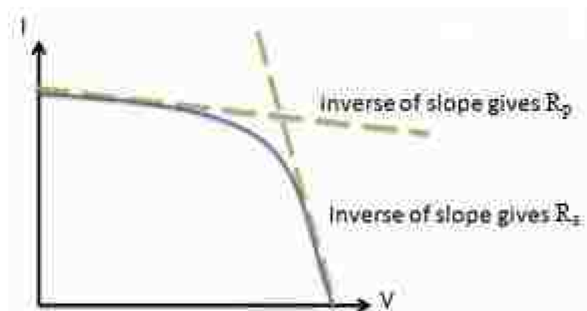

Figure 1.5 Series resistance and shunt resistance from IV curve. [6]

1.2.9 Solar cell spectral response

The spectral response of a solar cell is defined as the variation of the short-circuit current as a function of the wavelength of the incident light. To derive the equation of the

spectral response we use the one–dimensional model of the solar cell shown in Figure 1.6.

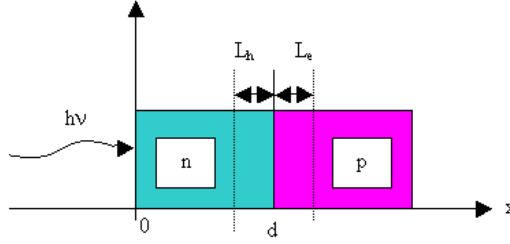

Figure 1.6 One-dimensional model of a junction solar cell.

The photon density generated in the material varies as:

$$\Phi = \Phi_0 \exp(-\alpha(\lambda)x) \quad (\text{sec}^{-1}.\text{cm}^{-2}) \tag{1.18}$$

where α is the absorption coefficient and d is the depletion region.

The electron-hole generation rate is then given by:

$$G(x) = \Phi_0 \alpha \exp(-\alpha x) \tag{1.19}$$

The total number of photogenerated carriers crossing the pn junction is given by [7]:

$$p_N^{op} + n_P^{op} = \frac{\Phi_0 \alpha}{\alpha + 1/L_h}\left[\exp\left(\frac{-d}{L_h}\right) - \exp(-\alpha d)\right] + \frac{\Phi_0 \alpha}{\alpha + 1/L_e}\exp(-\alpha d) \tag{1.20}$$

The above equation shows that, at longer wavelengths L_e and L_h must be large in order to obtain high photocurrent, due to the fact that α is small. This can be achieved by making the doping concentration low. However, lower doping will reduce V_{oc} as shown by equation 1.7. At shorter wavelength, α is high, therefore, d must be made small so that photons will be absorbed near the junction. Unfortunately, a smaller d will increase unwanted surface recombination thus the series resistance will increase; consequently the solar cell’s efficiency is reduced. This means the solar cell efficiency is limited by the device and design parameters.

1.2.10 External quantum efficiency

The number of electrons generated per photon, when a solar cell is illuminated, can be determined by calculating the external quantum efficiency (EQE) as given by equation 1.21.

$$EQE = \frac{1240 \times I_{ph}}{\lambda \times P_{in}} \qquad (1.21)$$

Where λ is the incident wavelength (nm), P_{in} is the power of the incident light (watt), and I_{ph} is the generated photocurrent (A).

1.3 Materials and Design Considerations

The materials used in the fabrication of solar cells must have bandgaps matching well with the sun's spectrum and also should have high carrier mobilities and long lifetimes. These parameters ensure that generated electron-hole pairs can reach the metal contact and contribute to the photo current. These requirements are met in semiconductor materials, such as Si, GaAs, GaInP, and Ge.

Non-ideal factors, such as series resistance and reflection from the semiconductor surface, will lower the conversion efficiency typically to the range of 10 to 15 percent. A large optical lens can be used to concentrate sunlight onto a solar cell so that the light intensity can be increased up to several hundred times. The short-circuit current increases linearly with light intensity while the open-circuit voltage increases logarithmically with intensity [8].

The two important external parameters that affect solar cells performance most are temperature and radiation effects. Since $L = \sqrt{D\tau}$, where L is the diffusion length, D is the diffusion coefficient, and τ is the carrier lifetime. As temperature increases, D

remains fairly constant or increases slightly, and τ increases. Therefore, the diffusion length L increases with temperature, causing an increase in I_{ph}. However since the saturation current increases exponentially with temperature, V_{oc} will decrease rapidly. The overall effect is a reduction of the cell's efficiency with increasing temperature.

1.4 Types of Solar Cells

From the above discussion, it is clear that for optimum solar cell performance, many tradeoffs should be considered. The most important parameter is the conversion efficiency. Improving the solar cell efficiency has been a challenge, which has inspired new and innovative ideas. This section will introduce three types of solar cells that demonstrate possible advancement toward higher efficiencies

1.4.1 Homojunction solar cells

The original design for the solar cell uses the homojunction. This is a pn-junction semiconductor of the same material [9]. Therefore, homojunction solar cells consist of only bulk material, which can absorb a limited portion of the sunlight spectrum. For example, if GaAs ($E_{g,GaAs}$ = 1.4eV) is the bulk material as shown in Figure 1.7, then the solar cell can only absorb light having a wavelength of 880nm and below. This means that wavelengths above 880nm are transparent to the material and do not contribute to the conversion efficiency.

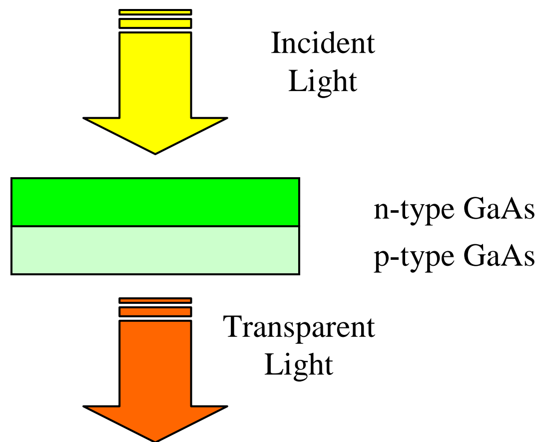

Figure 1.7 GaAs homojunction solar cell.

1.4.2 Heterojunction solar cells

When two different types of materials with dissimilar composition create a pn-junction, it is referred to as a heterojunction structure [10]. This type of structure is advantageous because now two band gaps are available so that one can act as an optical window, thereby reducing surface recombination. Heterojunction structures only require that the materials used should be closely lattice matched in order to reduce the effect of strain and dislocations. Strain and dislocations can greatly degrade the short circuit density, due to the carries being trapped rather than reaching the metal contacts. A closely lattice matched material system consist of GaAs/AlAs, which have a band gap offset of 0.73eV.

Figure 1.8 can be used to determine the suitable materials to fabricate heterojunction solar cells. One example is AlGaAs/GaAs solar cells, where AlGaAs is acting as an optical window and GaAs is the active layer that absorbs the solar spectrum.

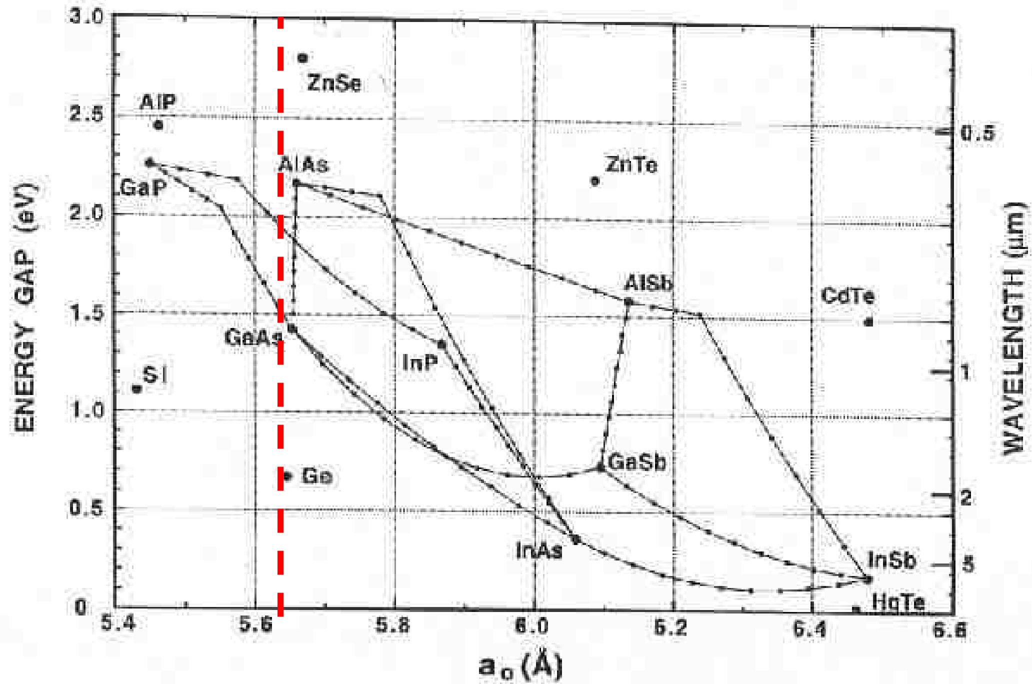

Figure 1.8 Lattice constant and bandgap of common semiconductor materials. [11]

1.4.3 Multijuction solar cells

To further enhance the absorption process, the multijunction structure was developed. Multijunction III-V-based solar cells can overcome the homojunction and heterojunction problems. Better absorption of the solar spectrum is achieved by using multiple semiconductor layers with different band gaps. The multijunction structure, also referred to as cascaded cells, can achieve higher total conversion efficiency by capturing a larger portion of the solar spectrum. In the typical multijunction cell, individual cells with different bandgaps are stacked on top of one another. These selective absorption processes continue through to the final cell, which has the smallest bandgap.

The difference between bandgaps of the multijunction should be made as small as possible in order to minimize heat dissipation due to excess energy. Three-junction solar cells currently in production are made of GaInP/GaAs/Ge [12] and GaInP/InGaAs/Ge

[13-15]. These systems have an efficiency as high as 27.5% and are usually for space applications, see Figure 1.9.

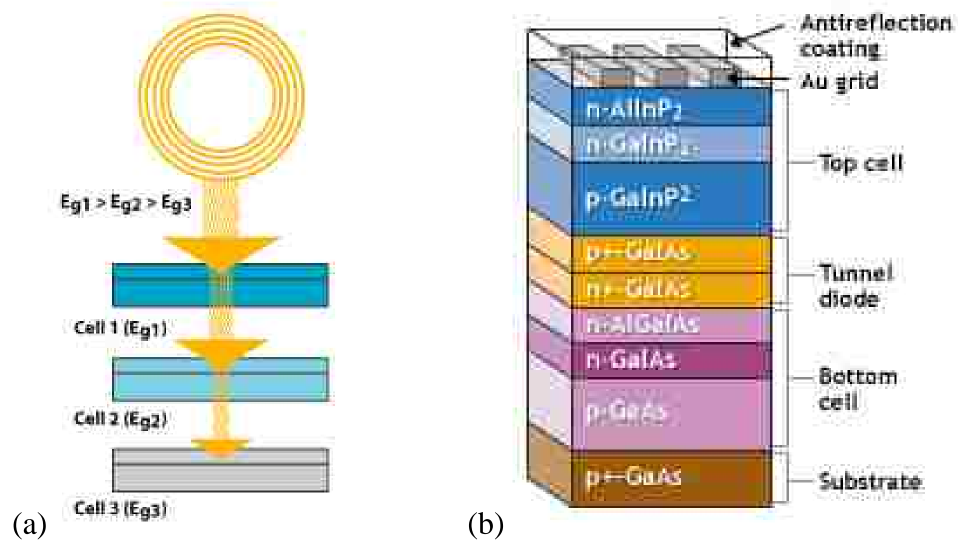

Figure 1.9 (a) Multijunction solar cell bandgap arrangement. (b)A structure of multijunction solar cell. [16]

1.5 Organization of Thesis

This chapter has given an introduction to solar cells, basic functions, operation, and different types. The chapters that follow will discuss more details pertaining to the thesis topic. Chapter 2 discusses the research review for QD solar cells. In this chapter motivation of the QD solar cell is explained. Chapter 3 describes the growth and structures of the samples used to carry out the experiments. Then the device fabrication is discussed in detail in chapter 4. The experimental setups and results are discussed in chapter 5. Chapter 6 will conclude with a summary of the thesis and presents future work research points.

CHAPTER 2 - Research Review

This chapter presents a brief summary and review of the published work entailing high efficiency solar cells. Recently new techniques have been developed to improve the conversion efficiency of solar cells.

2.1 Multijunction Solar Cells

One of the most efficient solar cells is a multjunction solar cell developed by Spectrolab [17]. These solar cells have recorded an efficiency of 40.7%, using a metamorphic (MM) three-junction GaInP/GaInAs/Ge cell, measured at 25°C and under AM1.5D. Figure 2.1 shows the measured I-V characteristics and the results obtained from metamorphic $Ga_{0.44}In_{0.56}P/Ga_{0.92}In_{0.08}As/Ge$ and lattice-matched $Ga_{0.50}In_{0.50}P/$ $Ga_{0.99}In_{0.01}As/$ Ge three-junction terrestrial solar cells.

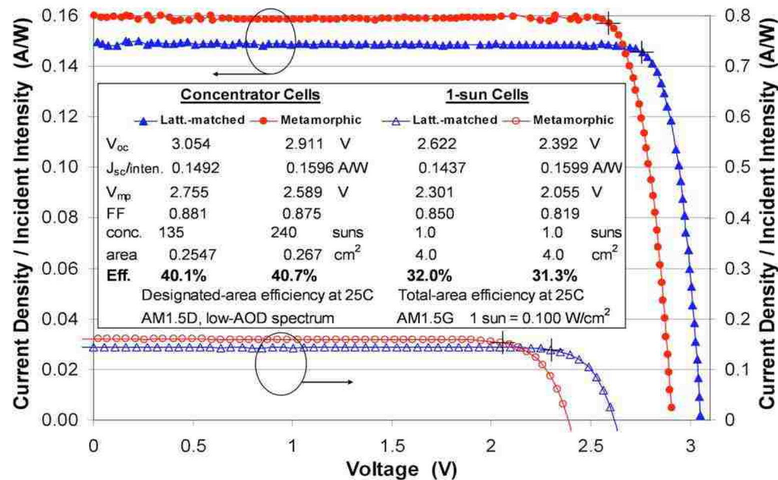

Figure 2.1 I-V Characteristic for metamorphic $Ga_{0.44}In_{0.56}$ $P/Ga_{0.92}In_{0.08}As/Ge$ and lattice-matched $Ga_{0.50}In_{0.50}P/Ga_{0.99}In_{0.01}As/Ge$ three-junction terrestrial solar cells. [17]

2.2 Intermediate Band Solar Cells (IBSC)

Another new technique currently under investigation is the Intermediate Band Absorption for Solar Cells (IBSC). This new approach was introduced by Luque *et al*. to enhance solar cell efficiency [18]. The idea behind this new approach is based on the absorption of low-bandgap energy photons by the intermediate band, which will increase photocurrent density and avoid voltage degradation. Figure 2.2 shows the energy band diagram for intermediate band absorption.

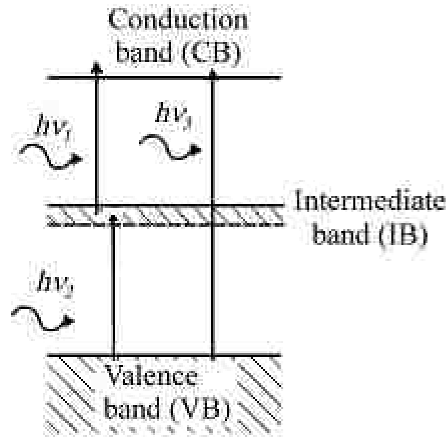

Figure 2.2 Schematic representation for Intermediate band absorption employed in solar cells structure to increase their conversion efficiency. [18]

In the intermediate band for solar cells a secondary material with bandgap (E_{g2}) smaller than that of the bulk material bandgap (E_{g1}) is used. This structure allows the secondary material to contribute to the absorption of an extra two photons, with energies ($hv_{1,2}$) less than the band gap of the bulk material, to generate an electron hole pair. In this model the intermediate band (IB) is often referred to as the metallic band because electrons must occupy half of the band in order to accept electrons from the valance band and to transfer electrons to conduction band of the bulk material.

The calculated efficiency for IBSC cells is obtained using the following assumptions:

- Non-radiative transitions are forbidden between any two bands.
- Infinite carrier mobility.
- Electrons are only extracted from the conduction band, holes are only extracted from the valence band, and no carries are extracted from the Intermediate band.
- The cell is made thick to absorb all photons.
- Radiation can only escape the cell from the front/top of the surface.
- The area considered in this model is unity.

Based on these assumptions Luque *et al*. were able to demonstrate that the efficiency predicted by Shockley and Queisser model can be exceeded [19]. Figure 2.3 shows the theoretically calculated efficiencies as a function of the intermediate bandgap energy.

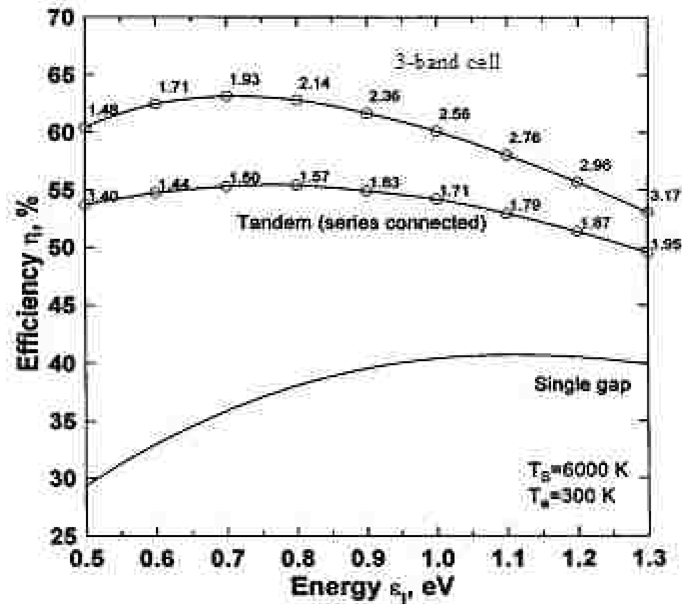

Figure 2.3 IBSC calculated theoretical efficiencies as a function of intermediate bandgap (IB). The single junction cells, and tandem cells are shown compared to the IBSC model. [1]

As can be seen in Figure 2.3 the conversion efficiency using intermediate band absorption can reach ~ 63.2% for PIN solar cells. Theoretically the main advantages of the IBSC are that the photocurrent and the open circuit voltage are higher than that of the single bandgap material. This design can be employed using either quantum well (QW) or quantum wire (QWR) or quantum dot (QD) layers as an intermediate bandgap material. In this study we investigated the use of InAs QDs as an intermediate bandgap material in GaAs-based solar cells.

2.3 Density of States

It is important to understand the difference between bulk material and quantum size structures in order to select an intermediate bandgap material for solar cells. In this section the density of the states, quantum size effect, and carrier confinement of quantum wells (QWs), quantum wires (QWs), and quantum dots (QDs) are discussed.

The density of states is defined as the probability distribution of the number of available states in each energy level that can be occupied by the carriers and it is given by [20]:

$$N = \int_{E_1}^{E_2} \rho_{DOS}(E)dE \qquad (2.1)$$

Where N is the total number of density of states per unit volume, ρ_{DOS} is the density of states per unit energy per unit volume; E_1 and E_2 are the bottom and top of the band, respectively. Figure 2.4 illustrates the density of states as a function of energy for the bulk material, quantum wells, quantum wires, and quantum dots. For bulk materials the carries are free to move in three dimensions (3D), for quantum wells carriers are allowed

to move in two directions (2D), for quantum wires carriers can only move in one direction, while for quantum dots carriers are confined in all direction (0D) so that there is no freedom of movement. This means using quantum size effect helps to improve carriers confinement while the concentration is reduced due to less density of states as the dimension gets smaller.

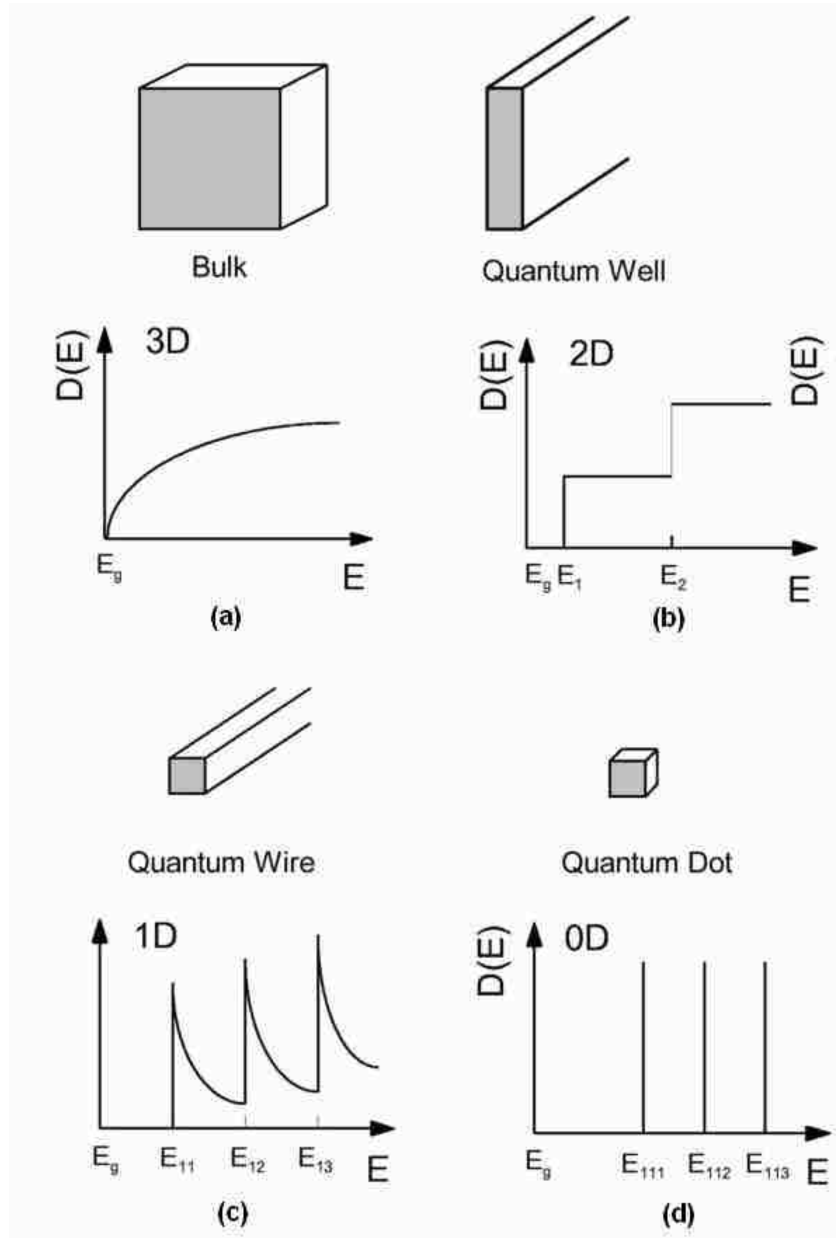

Figure 2.4 Semiconductor bulk, quantum well, quantum wire, and quantum dot structures density of states. [21]

The ability to grow QW, QWR, and QD such structures using MBE or MOCVD growth techniques has opened the door for new research and the application of such structures as intermediate low bandgap layers in solar cells.

2.4 Quantum Wells as Intermediate Band for Solar Cells

The QW was the first nano-structure applied in IBSC for low dimensional carrier confinement. Barnham *et al*. introduced the first QW pin solar cell structure in 1990 [22]. By inserting QWs in a pin solar cell structure as an intermediate band layer, the efficiency limit of 40.7% established by Shockley and Quiessser in 1961 would theoretically be surpassed.

In QW solar cells the absorption process can take place in different quantum energy levels by selecting the proper widths of the quantum well which in effect reduces the thermalization losses. Paxman *et al*. [23] have demonstrated that GaAs/AlGaAs QW pin structures can enhance both the short circuit current and conversion efficiency, in comparison with a control solar cell that has the same structure as the QW pin cell except without QW nanostructures. A simple diagram of a QW pin is shown in Figure 2.5, which demonstrates the different mechanisms that take place when a QW pin solar cell is illuminated.

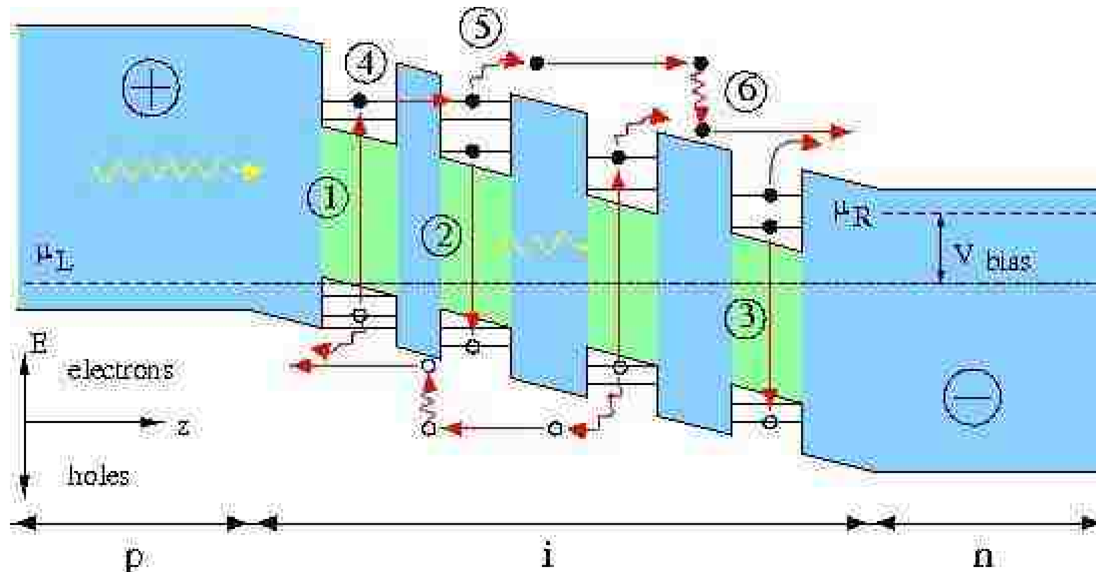

Figure 2.5 QW pin solar cell schematic operation. [24]

There are three main events that take place in the above schematic; electron-hole pair generation, electron-hole pair recombination, and carrier transport. However, the efficiency of IBSC can be reduced due to the involvement of several losses mechanisms such as: resonant and non-resonant tunneling, thermal escape and sweep out, and relaxation by inelastic scattering [24].

The main issue that arises when using quantum wells is that the density of states forms a continuum due to the continuous transverse freedom in two directions. Therefore, this allows for electrons in the conduction band and in the QWs to thermalize simply through phonon interaction phenomenon.

2.5 Quantum Wires as Intermediate Band for Solar Cells

Much of what is stated above applies to quantum wires (QWR). The primary difference involved with QWR structures it that they have one-dimensional freedom of movement for carries. This implies that the density of states forms a continuum due to the

continuous degree of freedom in one direction. Similar to QWs, the electrons in the conduction and well bands tend to thermalize simply through phonon interaction phenomenon. Therefore, to address this common problem in both QWs, and QWRs, complete carrier confinement is needed to limit the phonon interaction phenomenon. As a result, research entailing QDs as the IBSC has been recommended by Luque *et al*.

2.6 Quantum Dots as Intermediate Band for Solar Cells

Quantum dots (QD) on the other hand confine carriers in all three directions so that each carrier sits at a discrete energy state. This makes it difficult for the electron to thermalize by phonon interaction [25]. Thus quantum dots (QD) have many advantages if used as the intermediate band layer in solar cells. The wavelength at which the QD's can absorb or emit light can be tuned by adjusting the bandgap energy of the QD to the desired wavelength energy. This is implemented by changing the dot size. For example, if the dot size is large then the wavelength absorbed or emitted is relatively long. Quantum dots (QDs) can be grown in a three dimensional array with different stacking layers. As the number of layers of the dots increase, the size of the dot also typically increases. This implies that different QD sizes can absorb different wavelengths, allowing the cell to absorb more of the light spectrum, and thus improving the overall efficiency. Quantum dots (QDs) are also used to create more than one electron hole pair excitation from one photon. This process is called carrier multiplication (CM). For instance, if the energy of the incident photon is equal to two times the bandgap energy ($h\nu = 2E_g$), then two electron hole pair excitations can be generated. While in a bulk material only one electron hole pair excitation will occur, equivalent to the material bandgap energy. The remaining

excess energy will be dissipated in the form of heat, and lattice vibrations (phonons). In bulk materials, carrier cooling is a big problem which introduces Auger recombination. This process occurs in the picosecond range in bulk material. In quantum dots (QDs) the thermal relaxation is slowed down as a result of confinement, enabling hot carrier harvesting, and the reduction of electron hole interactions [26]. The advantage of QD CM is demonstrated in Figure 2.6.

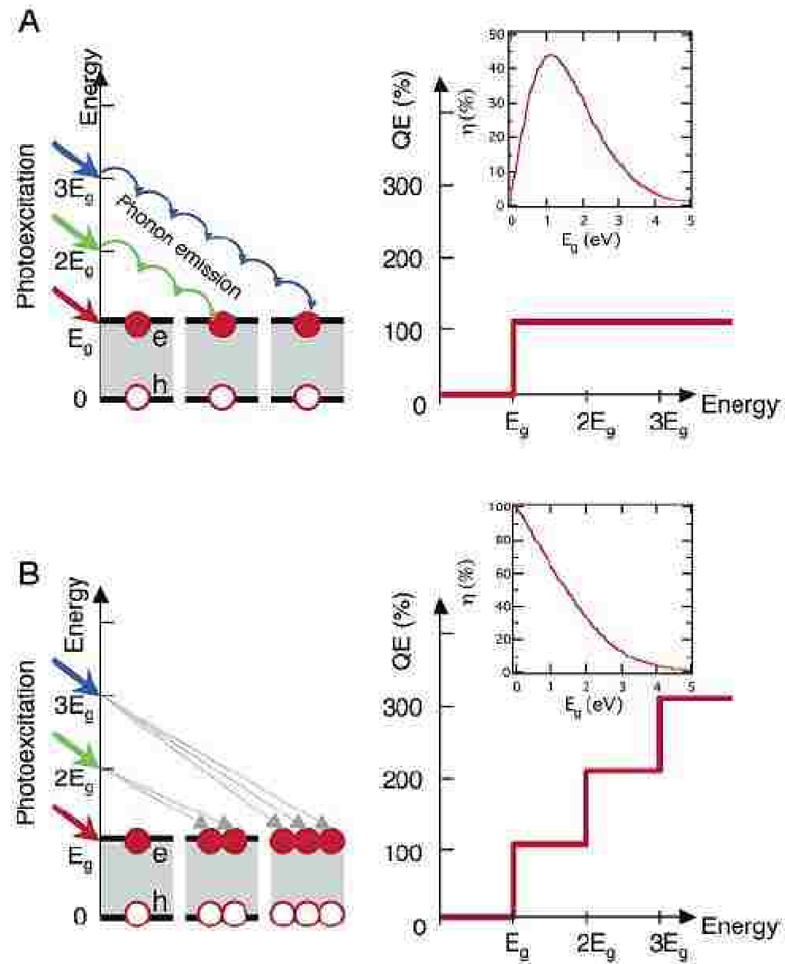

Figure 2.6 Carrier excitation demonstrated (A) without and (B) with carrier multiplication. [27]

2.7 Why QD IBSC?

It has been demonstrated the QD nano-structures enhance the photon absorption at longer wavelengths. Suwaree Suraprapapich *et al*. [28] incorporated InAs QD's into an GaAlAs/GaAs heterostructure and experimentally determined that QDs provide an additional spectral response at longer wavelength. This was also confirmed to be true by Samar Sinharoy *et al*. [29]. It has also been shown that increasing the QD stacks increases the spectral response of a solar cell as demonstrated by Seth Martin Hubbard *et al*. [30]. Consequently, the idea of embedding QDs in a material has also been extended to IBSC. Ever since Luque et al. [31] modeled IBSC and demonstrated that 63.1% conversion efficiency is possible, research has been under way in the area of using QDs to IBSC cells. The National Renewable Energy Laboratory (NREL) has carried out experiments utilizing InAs QD's as the IBSC, and reported photon absorption at longer wavelength.

It has been shown that QD can enhance the conversion efficiency, but more investigations are needed to study different QD effects, to better understand the trade offs entailed, and to determine the optimal structure design requirements. In this thesis InAs QDs as IBSC will be investigated to determine how QDs impact the operation of solar cells, and what new ideas can be implemented to achieve higher conversion efficiencies.

CHAPTER 3 - Solar Cells Material Structure and Characterization

This chapter discusses the structure and growth techniques for InAs QD solar cells. The photoluminescence (PL) measurements for the samples used will also be presented. The research samples are grown using molecular beam epitaxy (MBE) and metal organic chemical vapor deposition (MOCVD) crystal growth reactors at the Center for High Technology Materials (CHTM). Three unique samples were grown for this study, and are described by the following:

1. Run 2609: This sample was grown using MBE and is used as the GaAs-based control solar cell. This sample does not have QDs and has an undoped GaAs layer in the i-region. This sample is used as reference to compare with the QD samples.
2. Run 2611: This sample was grown using MBE and contains six-stacks of InAs QDs in the i-region. It is otherwise identical to 2609.
3. DE 3507: This sample was grown by MOCVD and contains three-stacks of InAs QDs in the i-region.

3.1 The PIN Diode

The solar cells used in this thesis are pin structures in which an intrinsic region (i-region) separates the heavily doped p-type and n-type regions. Figure 3.1 shows a schematic representation for the pin structure. In this design the electric field created between the n-type and p-type regions stretches across the intrinsic layer to increase the depletion region thickness and transport carries more efficiently by drift as opposed to diffusion. This is especially important for the QD regions because the dots could trap

carriers generated elsewhere in the device. In general, when the incident photons are absorbed in the intrinsic region, electron-hole pairs are generated. These carriers are then separated by the electric field and swept to the contacts. Once these photo-generated electrons and holes reach the neutral n- and p-type regions, respectively, they drift to the metal contacts and generate an external current. There are also photogenerated excess minority carries in the n- and p-type regions, which diffuse toward the i-region and then get swept across to the metal contacts.

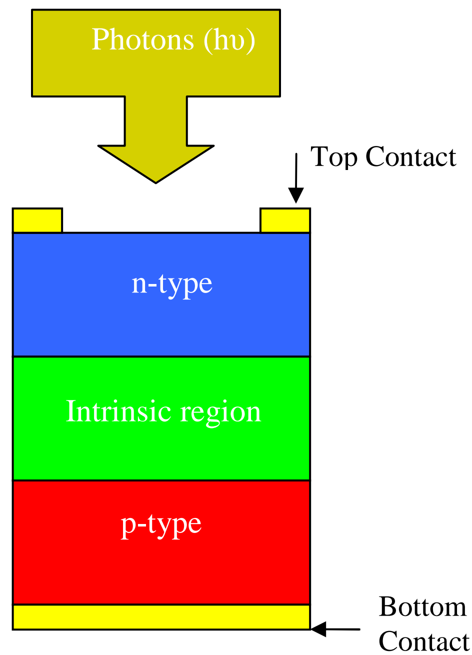

Figure 3.1 Schematic representation of the pin solar cell structure.

3.2 Energy Band Diagram of QD-based Solar Cells

Figure 3.2 illustrates the energy band diagram of QD solar cells grown on a GaAs substrate. In this figure $E_{c\text{-}GaAs}$ and $E_{v\text{-}GaAs}$ represent the conduction band and valance band for the GaAs material, respectively. As for the band gap of the InAs QD, it is represented by $E_{g\text{-}InAs\ QD}$. In this arrangement, the holes are confined in the valence band,

while the electrons are confined to the conduction band. The band offsets in this QD system are approximately 340meV and 100meV for the conduction band and valence band, respectively [32-34]. The intermediate band for solar cell (IBSC) model shows that this type of band alignment should yield a conversion efficiency of approximately 40%.

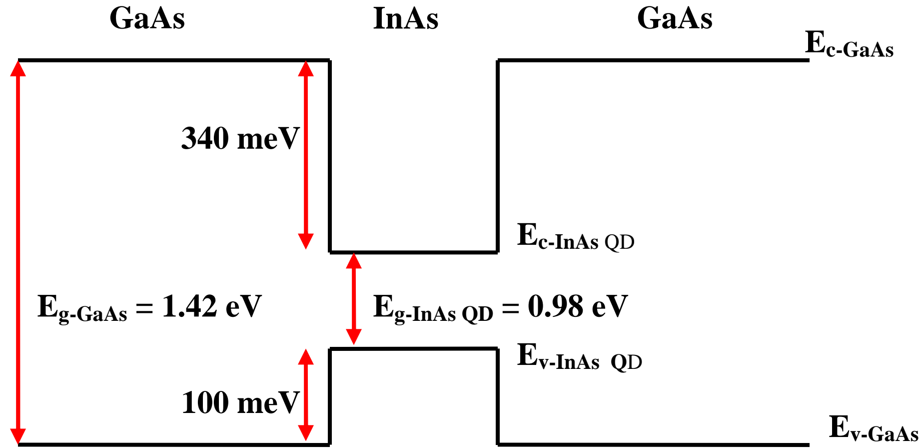

Figure 3.2 Energy band diagram for InAs/GaAs QD solar cell heterostructure.

3.3 Solar Cells Structures

The quantum dot solar cell samples tested in this thesis are grown by MBE and MOCVD. The control cell structure is similar to the QD structure except that there are no QDs. The total thickness of the intrinsic region in both the QD and control samples is kept the same, taking into consideration the QD wetting and cap layers and the average height of the quantum dots.

Figure 3.3 shows a schematic representation of both MBE structures. The control solar cell structure is illustrated in (A), while the 6-stack InAs QD solar cell structure is illustrated in (B). Figure 3.4 shows the MOVCD structure for the 3-stack InAs QD solar cell sample.

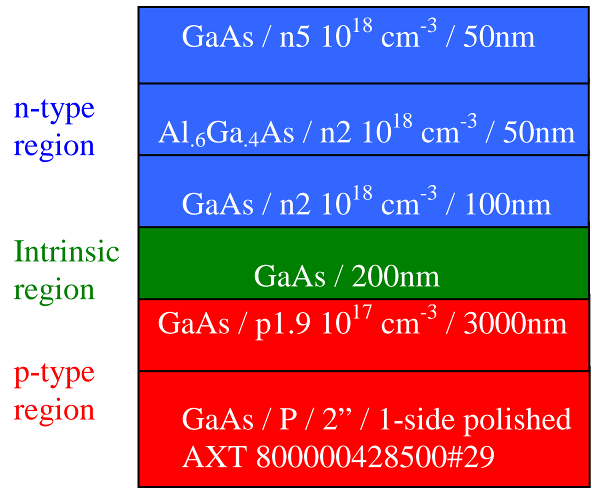

(A)

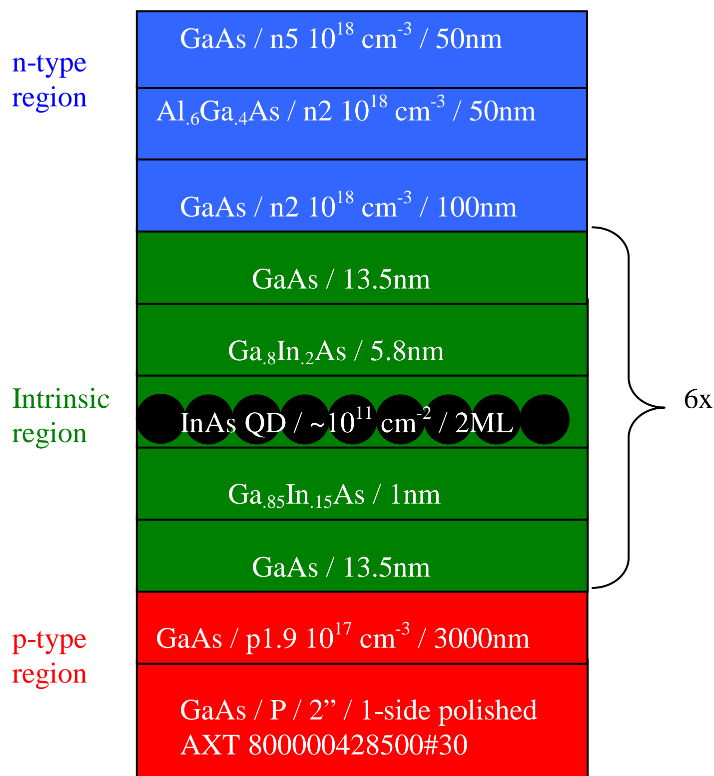

(B)

Figure 3.3 Samples structures of (a) MBE grown GaAs control cell, run2609 (b) MBE grown 6-stack InAs QD cell, run2611.

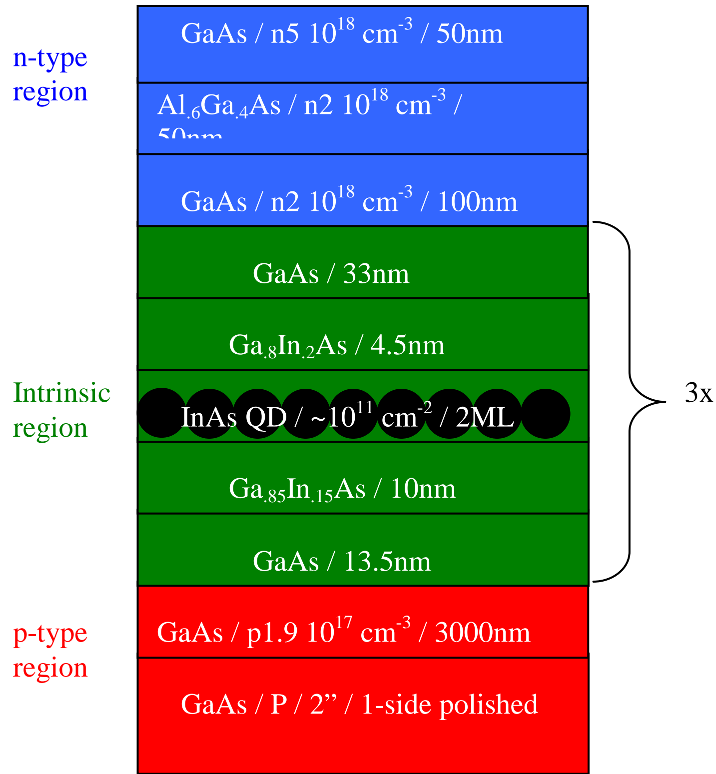

Figure 3.4 Samples structures of MOCVD grown 3-stack InAs QD cell.

The control cell is used as reference sample to study the effects of imbedding QDs in the GaAs pin junction and will be compared with the QD samples. Also in this study the performance of the solar cells grown by MBE is compared to the solar cells grown using MOCVD. The main difference between the two wafers is the technique used for the growth and the number of QD stacks. The MBE-grown sample contains six stacks of QDs while the MOCVD sample has three stacks. The I-V and spectral response measurements are presented and discussed in chapter 5.

3.4 Molecular Beam Epitaxy (MBE) Growth of Solar cells

Molecular beam epitaxy (MBE) is one of the crystal growth techniques used to deposit single crystal structures, with high quality, on a crystalline substrate. Briefly, the growth is carried out under ultra high vacuum and the substrate is heated to the desired temperature. The substrate is continuously rotated to establish a uniform layer thickness. The source materials are placed in effusion cells and the flux is controlled via shutters, which allows slow and precise deposition rates. Reflection high energy electron diffraction (RHEED) is used to monitor growth modes and growth rates [35]. A schematic representation of an MBE reactor is shown in Figure 3.5. This technique was utilized to grow two structures, which are run 2609 and run 2611. Each sample was grown on a two-inch diameter GaAs substrate wafer.

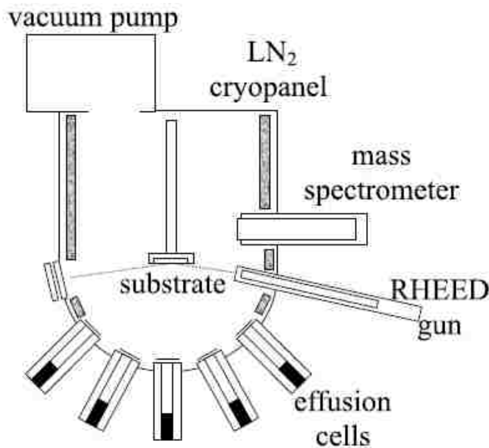

Figure 3.5 Schematic representation of a typical MBE chamber with five effusion cells and RHEED gun. [35]

3.5 Growth Characterization of MBE-Grown QDs

The MBE sample was grown by solid-source MBE in a Vacuum Generators V80H chamber. Silicon and beryllium were used for n- and p-doping, respectively. Arsenic was delivered in the form of the dimer As_2 from a valved cracker source. The

V:III beam-equivalent-pressure ratio used during growth of GaAs was about 7. Growth temperatures were between 580 and 620 ^{o}C for the (Al)GaAs layers and 470 ^{o}C for the GaInAs layer and the InAs quantum dots, as measured with an optical pyrometer [36].

Atomic force microscopy (AFM) is used to investigate the QD morphology. Figure 3.6 shows the AFM images of surface QD ensembles grown on an $In_{0.15}Ga_{0.85}As$ buffer layer at 470°C.

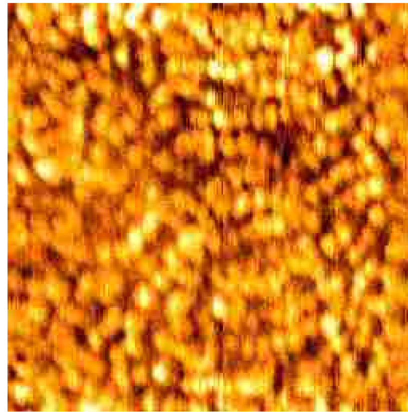

Figure 3.6 Atomic force microscope images of InAs QDs grown on $In_{0.15}Ga_{0.85}As$ buffer layers at 470° C. The scan size is 500 nm x 500 nm. [36]

Once the samples are grown, a photoluminescence (PL) measurement is performed. This measurement tests the photon absorption and emission of the substrate. The PL measurement is performed using a 3mW He-Ne laser. Figure 3.7 shows the PL measurements for samples 2609 (control cell) and 2611 (6-stack QD cell). The control cell and 6-stack QD cell demonstrate a PL response in the shorter IR wavelengths (800nm – 900nm), related to the GaAs contribution, with the control cell having a higher PL (0.006V at 870nm). At longer wavelengths (1000nm – 1180nm), only the 6-stack QD cell shows a PL response, which represents the effect of InAs QD PL contribution.

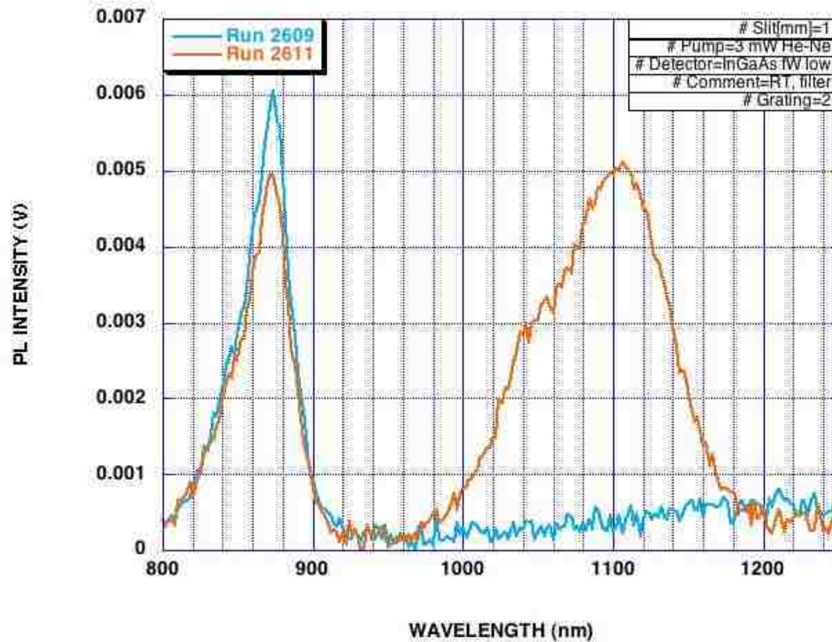

Figure 3.7 Photoluminescence measurement for sample run2609 (control cell) and sample run2611 (6-stack QD cell).

3.6 Metal Organic Chemical Vapor Deposition (MOCVD) Growth of Solar Cells

Metal organic chemical vapor deposition (MOCVD) is also another technique used to grow single crystal structures on a crystalline substrate. This method involves the use of a volatile gas, such as arsine (AsH_3) and one or more metal organics, such as trimethyl indium (TMIn) and trimethyl gallium (TMGa) to deposit different layers with different compositions, for example an InGaAs layer. A simple schematic representation of a typical MOCVD chamber is shown in Figure 3.8. This technique was used to grow sample DE3507, on a two-inch diameter GaAs wafer.

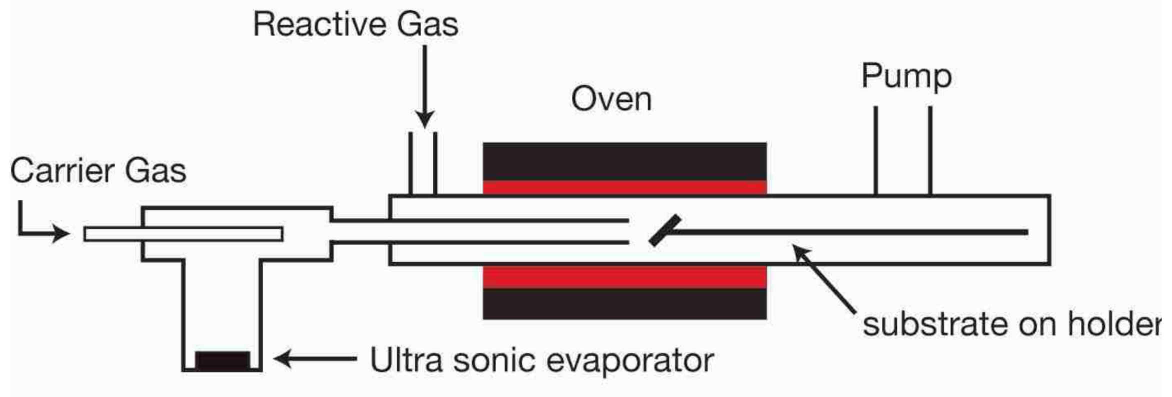

Figure 3.8 Schematic representation for a typical MOCVD chamber where source materials with carrier gas are mixed in the main manifold before the reaction takes place in the chamber. [37]

3.7 Growth Characterization of MOCVD-Grown QDs

The samples are grown in a Thomas Swan vertical MOCVD reactor at 60 Torr. Before growth, semi-insulating GaAs (100) substrates are deoxidized at 760 °C for 5 min. A 3000 Å p-GaAs layer is grown at 680 °C then the temperature is lowered and stabilized for QD growth within the range of 450 °C to 520 °C. The wetting layer, QDs, and capping layers are grown at the same temperature. For all samples, the wetting and cap layers are $In_{0.15}Ga_{0.85}As$. The QDs are capped with 45 Å $In_{0.15}Ga_{0.85}As$ and 330 Å GaAs layers also grown at the same temperature. After QD growth, the temperature is raised to 570 ^{o}C to grow n-type GaAs. n-AlGaAs layer and n-GaAs cap layers are grown at 630 ^{o}C. The growth rate and V/III ratio are kept constant at 0.5 ML/s and 52.5, respectively, during QD growth.

Figure 3.9 shows the AFM images of surface QD ensembles grown on an $In_{0.15}Ga_{0.85}As$ buffer layer at 500 ^{o}C. From AFM scans, the dot density is $8x10^{10}$ cm^{-2} with an average height of 25 Å.

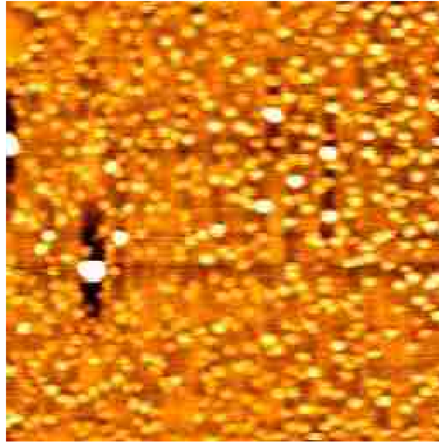

Figure 3.9 Atomic force microscope images of InAs QDs grown on $In_{0.15}Ga_{0.85}As$ buffer layers at 500° C. The scan size is 1 μm x1 μm. [38]

Figure 3.10 shows the room temperature PL spectrum from capped QDs on $In_{0.15}Ga_{0.85}As$ at 500 ^oC. The QDs are formed under the same conditions as those shown in Figure 3.9. The PL peak wavelength is observed at 1.34 μm with a narrow linewidth of 40 meV. A significant blue-shift and a narrow FWHM result from the covering process. Because the overgrowth takes place at the QD growth temperature, any intermixing of In and Ga atoms is primarily strain-induced and results in increased uniformity of QD size and composition [38].

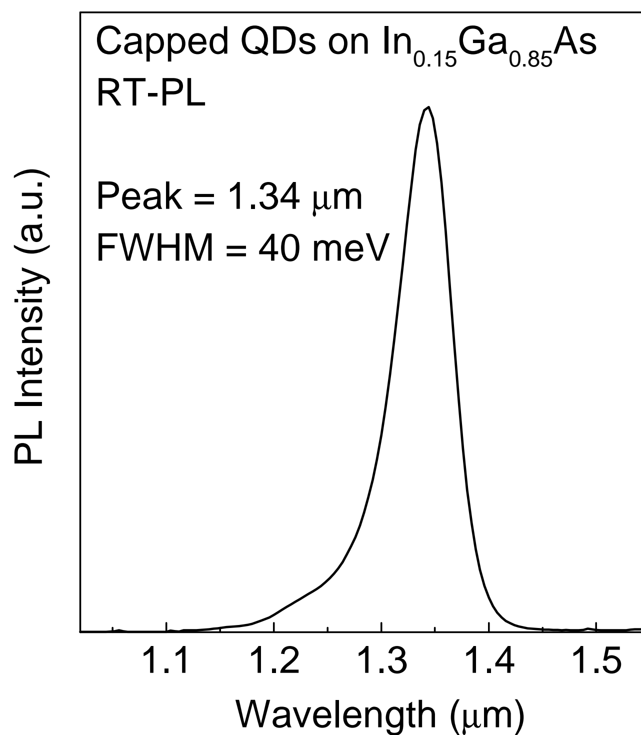

Figure 3.10 Room-temperature PL spectrum of capped InAs QDs grown on $In_{0.15}Ga_{0.85}As$ at 500° C. The cap layers, grown at 500 ℃, are 45 Å of $In_{0.15}Ga_{0.85}As$ and 330 Å of GaAs.

CHAPTER 4 - Solar Cells Processing and Fabrication

This chapter presents the processing and fabrication steps for the three different solar cells structures: the GaAs control cell, the MBE grown six-stack QDs solar cell, and the MOCVD grown three-stack QDs solar cell. All wafers are processed using the fabrication tools in a class 1000 clean room at the Center for High Technology Materials.

After the solar cells structures are grown, the wafers are processed using two different methods for processing, which feature the following key differences:

1. Inductively coupled plasma (ICP) etching without sidewall passivation of the cell.
2. Wet etching with silicon nitride sidewall passivation.

Both procedures are used to study the effect of processing on the performance of solar cells. In the first method, the ICP etch is used for device isolation without passivating the sidewalls of the mesa structures. In the second method, wet chemical etching is used for device isolation and the sidewalls of mesa structures are passivated. The effect of both methods is observed and presented in chapter 5.

Since solar cells structures are grown on 2-inch wafers, this area is more than sufficient for processing the 2x2mm, 3x3mm, and 5x5mm square cells studied. Therefore the full wafer is cleaved and only one quarter is used for processing and the other three quarters are kept for later use, if we needed.

4.1 Sample Preparation Fabrication Steps

Before processing, the wafer is cleaned and by soaking it in acetone, methanol, and isopropyl alcohol (IPA) baths, for five minutes in each solution. Then the native oxide is removed from the surface using a basic solution of ammonium hydroxide and deionized water ($NH_4OH:H_2O$) with ratio 1:30, respectively, for 30 seconds. Then the sample is baked at 150^oC for 10 minutes. This step is the dehydration bake, since moisture is removed from the wafer surface.

In the following sections, I will discuss two methods for mesa isolation using inductively coupled plasma (ICP) etching without sidewall passivation and wet etching with sidewall passivation.

4.2 Inductively Coupled Plasma (ICP) Etching without Sidewall Passivation

At this point the sample is ready for processing. Figure 4.1 shows a schematic representation and a flowchart for the processing steps using the inductively coupled plasma (ICP) etching technique and without sidewall passivation.

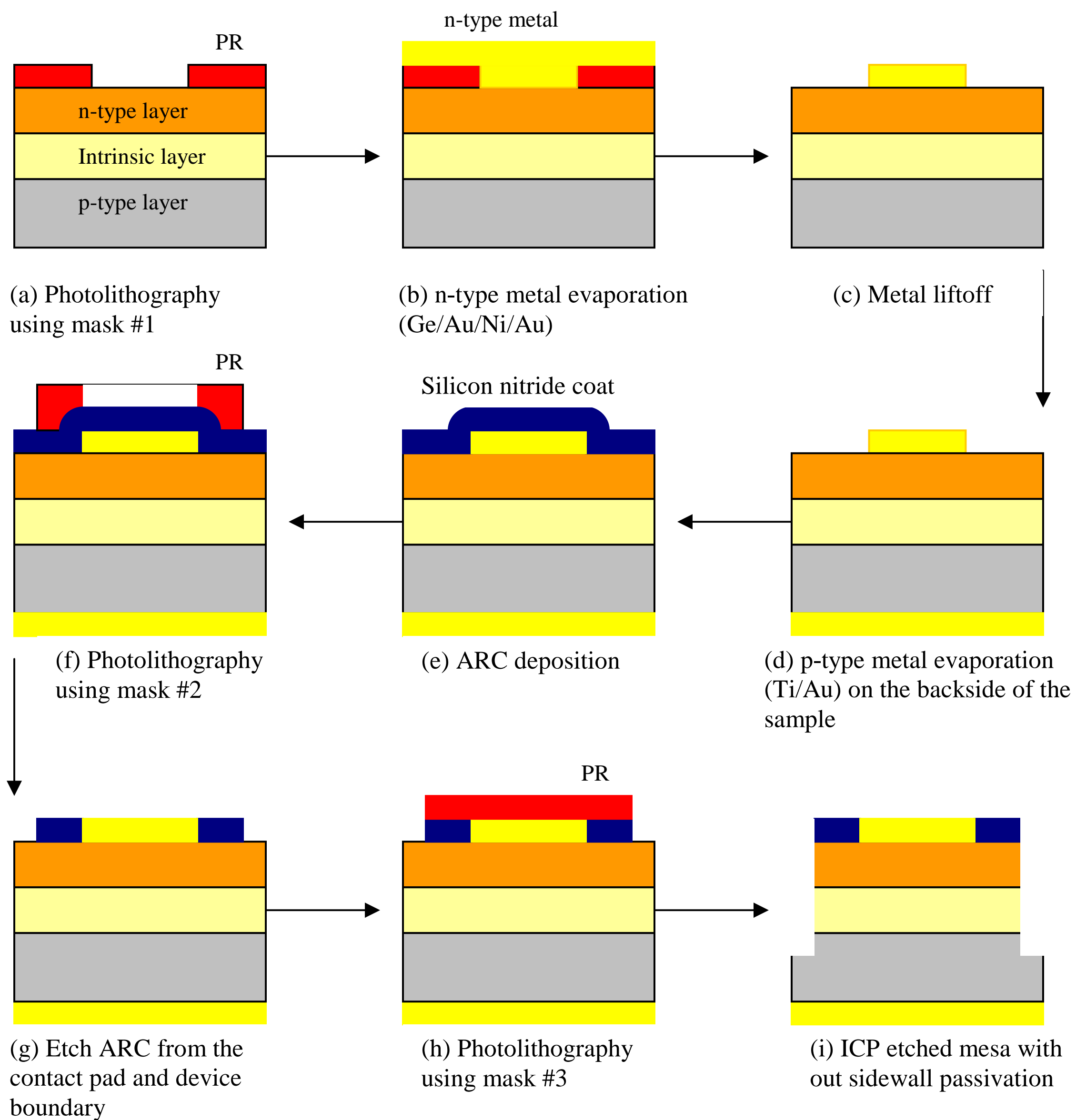

Figure 4.1 Schematic representation of the processing steps using inductively coupled plasma (ICP) etching without sidewall passivation.

To ensure smooth surface preparation, hexamethyldisilazane (HMDS) is applied on the sample surface, using a spinner at 4000 rpm for 30 seconds. HMDS is used as an adhesion promoter before photoresist is applied. Then the sample is baked at 150 ^{o}C for 3 minutes. The wafer is then coated with a positive photoresist type AZ5214E-IR using a

spinner at 4000 rpm for 30 seconds. After the PR coat, the sample is soft baked at 90 ^{o}C for 2 minutes to remove excess solvent PR.

Now the sample is ready for the first photolithography step. Using the mask aligner the sample is exposed with ultraviolet (UV) light at 365nm wavelength for 5 seconds. A photograph for the solar cell mask #1 used in this process is shown in the Figure 4.2. This mask has three different sizes of square solar cells with dimensions 5x5mm, 3x3mm, and 2x2mm.

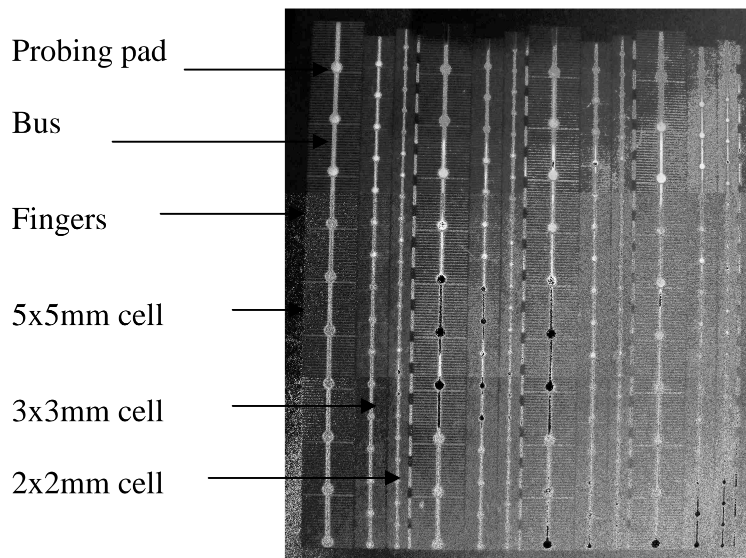

Figure 4.2 Photograph of mask 1 for the solar cell patterns. Three different areas are shown 5x5 mm, 3x3 mm, and 2x2 mm. Metallization of probing pad, bus, and fingers are also shown for the three different solar cells.

Once the exposure is complete the sample is baked at 112 ^{o}C for 1 minute to reverse the image. To activate the photochemistry, the full wafer is then exposed to the UV light without the mask (flood exposure) for 1 minute at 365nm. The sample is then developed for 20 seconds in a solution of AZ400K developer and deionized water with a ratio of 1:5, respectively. Figure 4.1 (a) shows an illustration of the wafer after

developing. After this step a replicated image of the solar cell mask #1 is printed on the wafer.

The sample is then prepared for the top n-type ohmic contact metal evaporation. Before metal evaporation, oxygen plasma exposure is performed, using a reactive ion etcher (RIE) for 1 minute to remove any unwanted photoresist scum. The native oxide is also removed using a solution of $NH_4OH:H_2O$ with a ratio of 1:30. Using an electron beam for metal evaporation, the top n-type ohmic contact metal is evaporated on the surface as shown in Figure 4.1 (b). This n-type contact layer consists of Ge/Au/Ni/Au with thicknesses of 260Å, 540Å, 200Å, and 3000Å, respectively. This metallization process covers ~ 20% of the solar cell surface area and creates a shadowing effect on the surface.

The sample is then placed in an acetone bath overnight for metal liftoff. This allows the acetone to dissolve the PR remaining on the sample, and to remove the metal on top of the PR. Therefore, the only remaining metal on the sample is the top n-type ohmic contact layer, which corresponds to the metal pad, metal bus, and metal fingers as shown in Figure 4.1 (c).

The bottom p-type ohmic contact metal is then evaporated on the backside of the sample. This is done by mounting the sample upside down on a dummy silicon wafer, using PR to stick the sample to the silicon wafer. The p-type contact layer consists of Ti/Au (500Å/3000Å). An acetone bath is then used to free the sample from the silicon wafer after the back surface metal evaporation, as shown in Figure 4.1 (d).

The sample is cleaned using reactive ion etcher (RIE) for 3 minutes. Rapid thermal annealing (RTA) is then used to heat the sample for 60 seconds at 380 ^{o}C. This makes a good ohmic contact with the sample.

In order to minimize the light reflection at the top surface of the solar cell an antireflection coating (ARC) of silicon nitride (Si_3N_4) is deposited, as shown in Figure 4.1 (e). This AR coating is deposited using plasma enhanced chemical vapor deposition (PECVD), with a thickness of approximately 1000 Å and a 2.05 index of refraction. To probe the solar cell for characterization, the AR coating on the contact pads must be removed. This is done via photolithography, see Figure 4.1 (f). The photolithography steps are the same as mentioned above and the only difference is the mask used. A photograph of the second photolithography mask is shown in Figure 4.3.

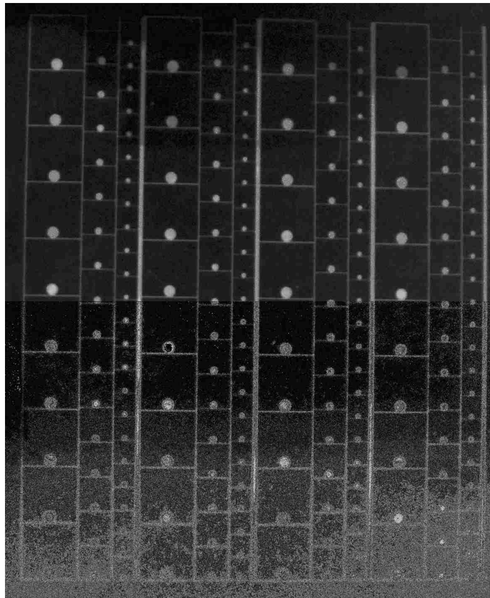

Figure 4.3 A photograph of mask #2 used to remove antireflection coating from the contact pad and the solar cell boundary.

This mask is used to remove silicon nitride on the contact pad and the cell boundaries, as shown in Figure 4.1 (g). The Si_3N_4 on the pads and boundaries can then be

etched using the RIE at a partial pressure of 45 mtorr, CF_4, and 255 mtorr, O_2, for 3 minutes.

To isolate solar cells from each other, a third photolithography step is performed, as shown in Figure 4.1 (h, i). A photograph of mask # 3 is shown in Figure 4.4.

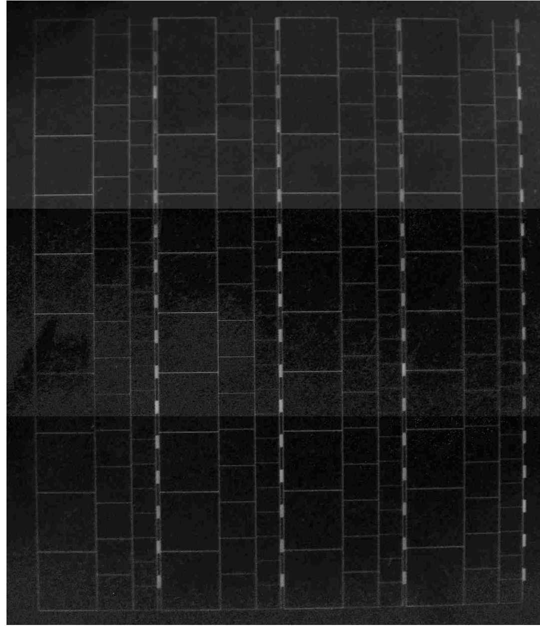

Figure 4.4 A photograph of mask #3 used to identify the final mesa solar cell structure.

Etching the mesa structure is then performed using boron trichloride gas (BCl_3) in the inductively coupled plasma (ICP) chamber. The boron trichloride gas used in the ICP etches the GaAs surface, which is not covered by PR. This type of etching leaves a rough GaAs surface with dangling bonds and surface defects. The non-passivated mesa sidewalls in this case can greatly affect the solar cell short circuit current by increasing surface recombination. This observation is reported in chapter 5.

Once the ICP etch is completed, the sample is cleaned with IPA and deionized water. The sample is then ready for characterization. Figure 4.5 shows a photograph of

the final product and a sketch of the etched mesa. In this figure the ARC layer (Si_3N_4) is clearly shown by the navy blue color on the sample surface.

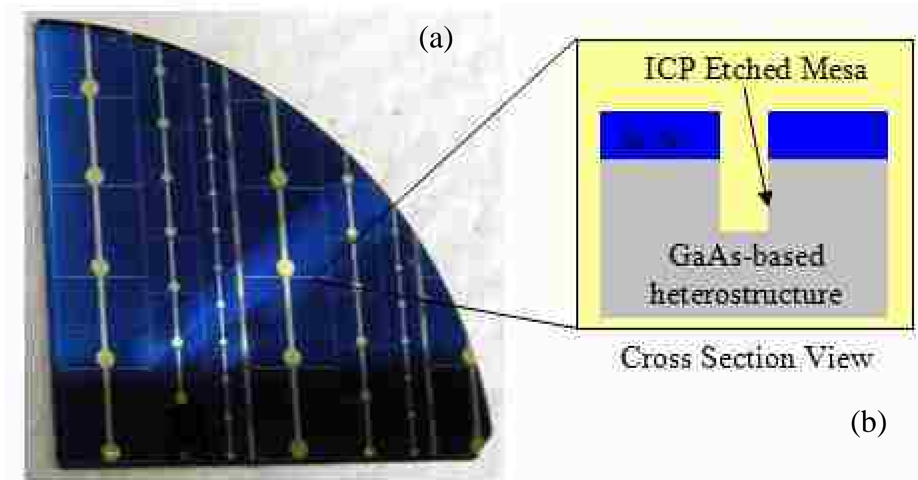

Figure 4.5 (a) Processed quarter wafer (b) Cross-sectional view of mesa structure.

4.3 Wet Etched Mesa with Sidewall Passivation

In this technique the first photolithography step is similar to that discussed in section 4.2, as shown in Figure 4.6 (a-d). To identify the boundaries of the mesa structure, photolithography is performed using mask #3, see Figure 4.6(e). In this case the solar cell boundary lines will not have PR, while the rest of the sample will be covered with PR. This etching step is carried out using a wet etch acid solution consisting of phosphoric acid, hydrogen peroxide, and deionized water (H_3PO_4:H_2O_2:H_2O) with ratios 3:1:50, respectively at an etch rate of 13.5 Å/sec. This type of etching leaves a smooth GaAs surface and etches specific planes with different etch rates. Figure 4.6(f) shows the mesa structure after etching the sidewalls.

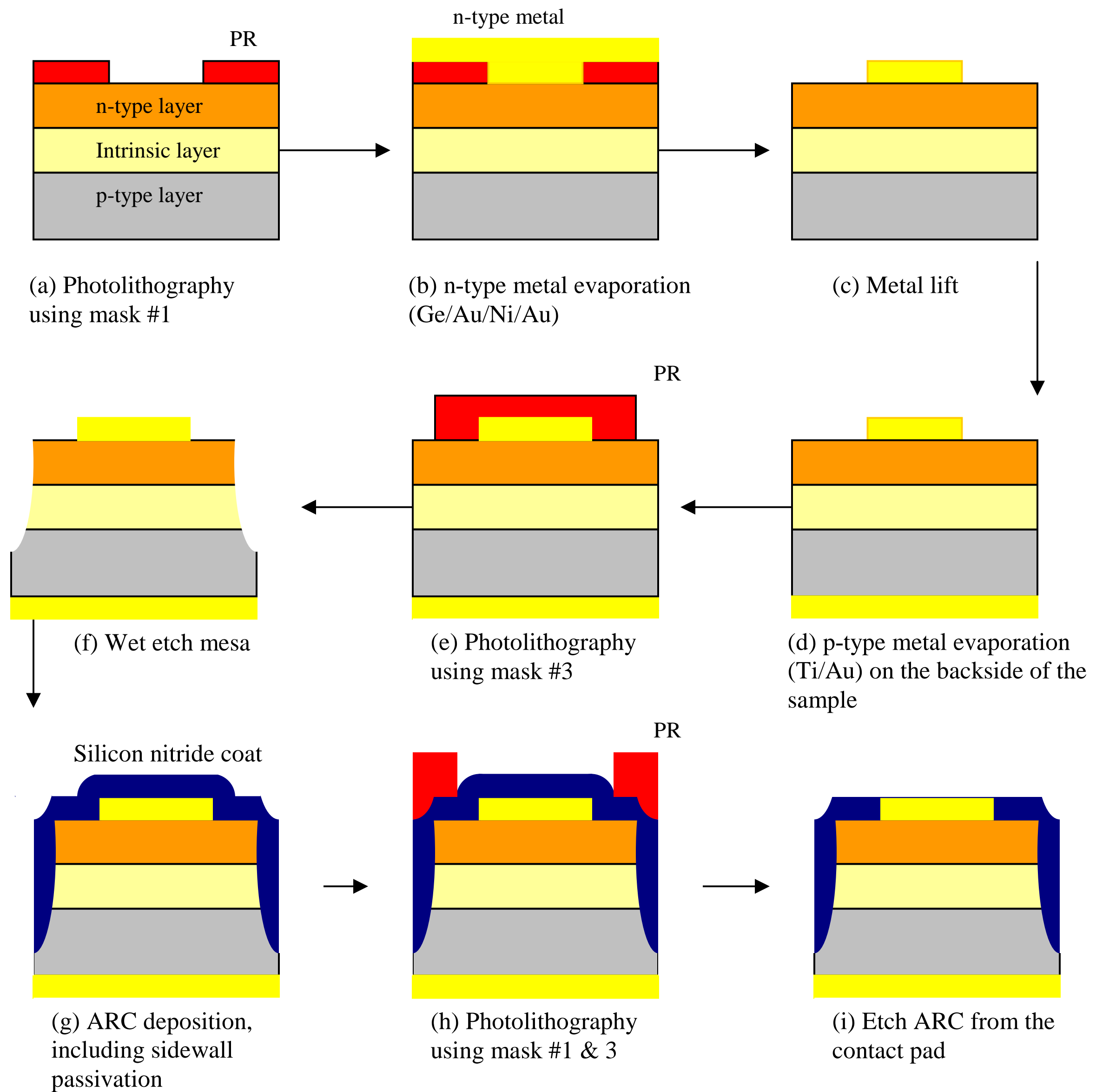

Figure 4.6 Schematic representation for the processing steps using wet etching with sidewall passivated mesa structure.

A 1000Å ARC with a 2.05 index of refraction is then deposited on the sample using the PECVD, as shown in Figure 4.6(g). Then silicon nitride on the contact pads is defined using masks 1 and 2, as illustrated in Figure 4.6(h). Both masks #1 and #2 are

used in this photolithography step to expose silicon nitride on the contact pads only. Reactive ion etching is then used to remove the silicon nitride from the top surface of the contact pads as shown in Figure 4.6(i). Both ICP and wet etching processes show similar mesa structures with the only difference being the sidewall passivation as shown in Figure 4.7.

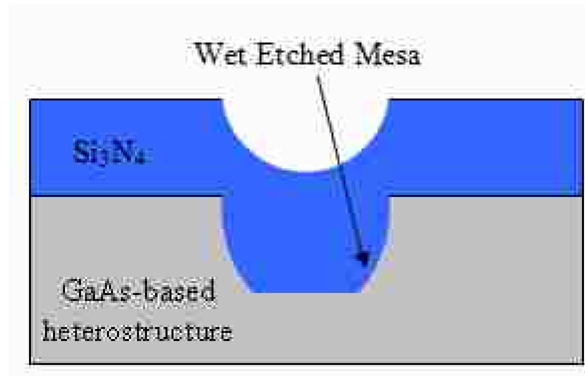

Figure 4.7 Cross-sectional view of wet etched mesa structure.

CHAPTER 5 - InAs QD Solar Cells Characterization

This chapter presents the measurements and characterization of InAs quantum dot solar cells. These devices are tested and the results are discussed to understand the effects of introducing InAs QDs, as a potential intermediate band material for solar cells.

5.1 Device Characterization

Solar cell performance is measured using I-V characterizations and spectral response measurements. Two setups are used to carrier out the above measurements and are explained in the following sections.

5.1.1 I-V Experimental Setup

The I-V setup is used to measure the current-voltage characteristics of solar cells with light illumination and under dark conditions. From these measurements we can deduce many solar cell parameters such as: short circuit current (I_{sc}), open circuit voltage (V_{oc}), maximum power, cell efficiency, series resistance, shunt resistance and ideality factor. Therefore, the I-V measurement is important for solar cell characterization. Figure 5.1 shows a schematic representation for the experimental setup used to measure the I-V curves of solar cells.

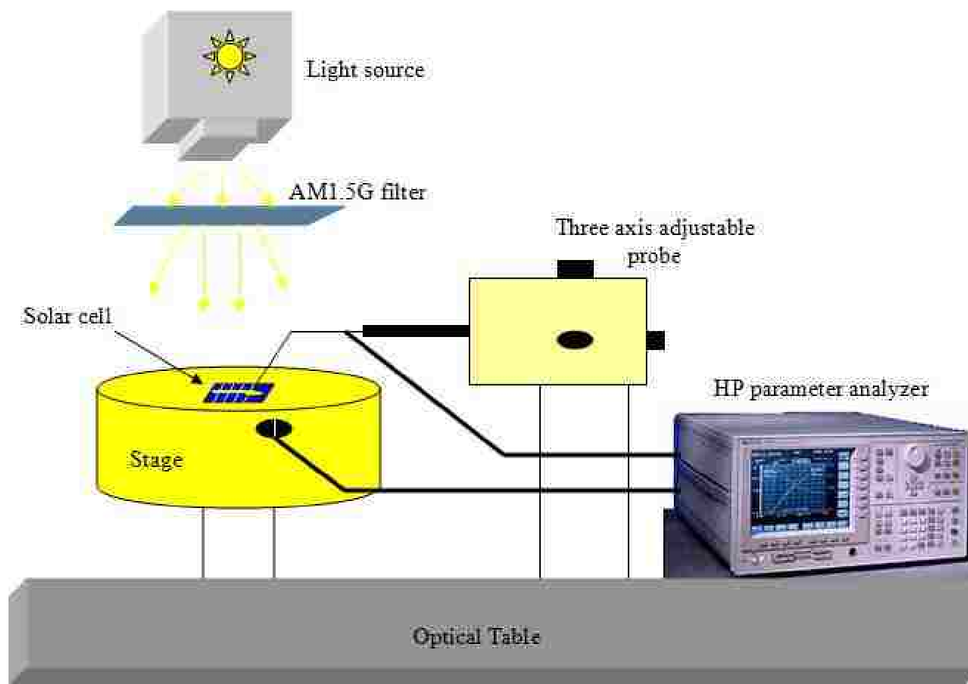

Figure 5.1 A schematic representation of the setup used to measure the I-V characteristics of solar cells.

The setup consists of an ABET Technologies light source, with a 150 watt xenon lamp simulating sun light. A filter is inserted between the light source and the sample stage to emulate sun light intensity and irradiance. For example AM0D (air mass zero with direct incidence with no scattering) and AM1.5G (air mass 1.5 global with direct incidence and diffused light) can be obtained by changing the filter. In this study AM1.5G filter is used. The distance between the light source and the sample is adjusted so that light with intensity 100.0mW/cm^2 (1 sun) is hitting the solar cell surface. This intensity was measured using an EPM 1000 power meter with a PM3 detector. Since the top layer of the solar cell is n-type, the top contact of the sample represents the negative terminal while the positive terminal is attached to the stage. A Hewlett Packard 4155B parameter analyzer is used to collect the I-V data. This is done by sweeping the voltage

from -1V to 1V in steps of 10mV and measuring the current. The data is then saved and plotted using Igor Pro for analyses.

5.1.2 Spectral Response Experimental Setup

The spectral response measures the photocurrent's wavelength dependence. Therefore, the GaAs control solar cell and the InAs QD solar cells can be compared. Figure 5.2 shows a schematic representation of the setup used to measure the spectral response of the solar cells.

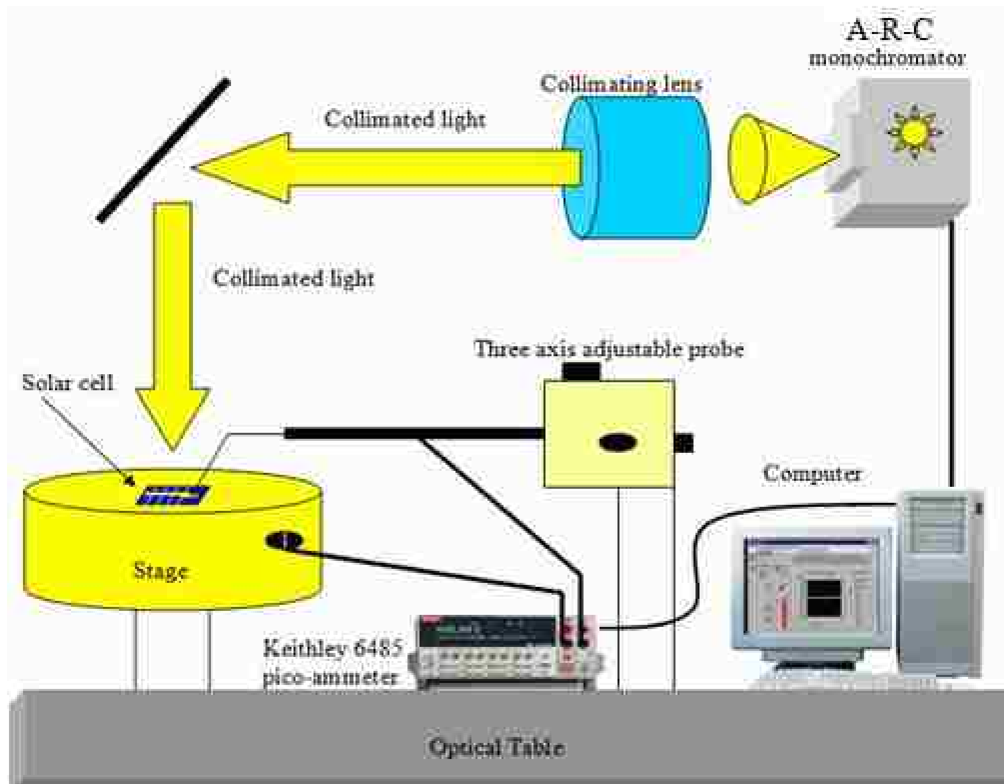

Figure 5.2 A schematic representation of the setup used to measure the spectral response characteristics for solar cells.

This setup consists of an Acton Research Corporation (A-R-C) monochromator with a 250 watt tungsten lamp. The monochromator has gratings to select a specific

wavelength range required for the experiment. The light exiting the monochromator is collimated using a lens and steered to the probing stage using free space mirror alignments. In this experiment the monochromator scans the wavelength range from 400nm to 1300nm. The Keithley 6485 pico-ammeter is used to measure photocurrent for each wavelength. Both the monochromator and pico-ammeter are computer-controlled using Labview7.1.

5.2 Characterization of ICP Etched-Mesa Solar Cells Fabricated without Silicon Nitride Sidewall Passivation

This section presents the measurements of the 5x5mm solar cells grown by MBE and MOCVD techniques. These solar cells are fabricated simultaneously under the same processing conditions, using ICP etching without silicon nitride sidewall passivation. The following wafers are characterized:

1. The GaAs MBE control solar cell (run 2609)
2. The MBE 6-stack InAs QD solar cell (run 2611)
3. The MOCVD 3-stack InAs QD solar cell (DE 3507)

5.2.1 I-V Measurements of the ICP etched solar cells without silicon nitride sidewall passivation

Figure 5.3 shows the I-V characteristics for the 5x5mm control cell, six stack, and three stack solar cells.

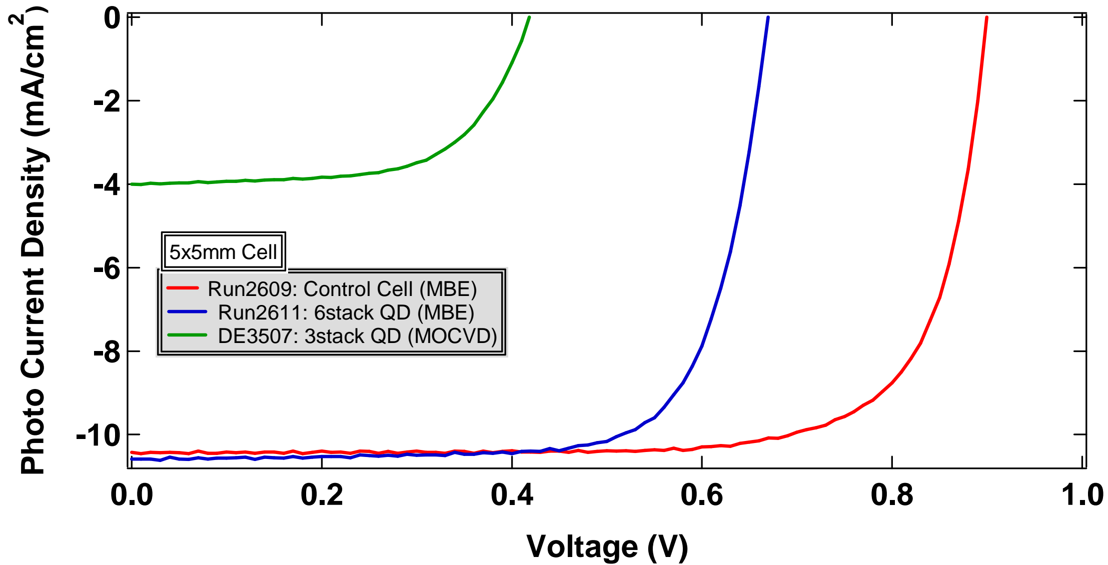

Figure 5.3 I-V characteristics for the 5x5mm ICP etched and unpassivated mesa solar cells. Control (red), 6-stack InAs QD (blue) and 3-stack InAs QD (green) solar cells processed under the same conditions.

The data extracted from this figure show that the control cell (red line) has an open circuit voltage (V_{oc}) of 0.90V and a short circuit current density (J_{sc}) of 10.4mA/cm^2. It has been reported that the open circuit voltage of GaAs-based solar cells is ~1V, indicating a good agreement with the results presented here. Also as shown in Figure 5.3 the 6-stack InAs QD solar cell has an open circuit voltage (V_{oc}) of 0.67V and a short circuit current density (J_{sc}) of 10.6mA/cm^2. The decrease in the open circuit voltage for the 6-stack InAs quantum dot solar cells compared with the control cell may be due to either the relaxation of quasi-fermi-levels close to the QD conduction and valance band or the material is slightly degraded by quantum dots. Both mechanisms may introduce this effect. Figure 5.3 also shows a slight increase in the short circuit current density of the 6-stack InAs QD compared to the control solar cell. This increase of J_{sc} is most probably due to higher photon absorption rate related to the InAs QD layers. Luque *et. al*

predicted that the intermediate band for solar cells would increase the conversion efficiency [39] by maintaining the V_{oc} and increasing J_{sc}.

For the MOCVD 3-stack InAs QD solar cell, as shown in Figure 5.3, the measured open circuit voltage (V_{oc}) is 0.42V and the short circuit current density (I_{sc}) is 4.00mA/cm^2. These lower values, compared to the MBE 6-stack InAs QD solar cell, may be attributed to many mechanisms such as: fewer QD layers with different physical and electrical properties, thinner i-region, and/or less material quality. This interpretation needs further investigation.

To study the performance of these solar cells, their data are collected from Figure 5.3 and summarized in Table 5.1. This table shows that the conversion efficiencies of the GaAs control solar cell, and of the six-stack InAs QDs solar cells, and the MOCVD three- stack InAs QD solar cells are: 8.95%, 6.55%, and 1.33%, respectively, including having removed the shadowing effect from the metal fingers.

	MBE grown wafers		MOCVD grown wafers
	Run 2609: Control Cell	Run 2611: 6-stack QD	DE3507: 3-stack QD
Short Circuit Current Density (mA/cm^2):	10.4	10.6	4.00
Open Circuit Voltage (V):	0.90	0.67	0.42
Normalized P_{max} (mW/cm^2):	7.16	5.24	1.06
FF (%):	76.5	73.8	63.1
Efficiency (%):	8.95	6.55	1.33
Normalized Series Resistance ($\Omega.cm^2$):	0.560	0.925	0.935
Normalized Shunt Resistance ($k\Omega.cm^2$):	12.6	6.70	1.98
Ideality Factor (n):	2.71	1.85	1.97
Normalized Saturation Current (nA/cm^2):	2.07	5.04	542

Table 5.1 Data summary for the 5x5mm control, 6-stack InAs QD and 3-stack InAs QD solar cells fabricated by ICP etching and without sidewall passivation.

These efficiencies are calculated using equation 1.15 where the 20% shadowing effect, of the top surface metal contacts, is accounted for. As clearly seen from Table 5.1, the control cell has the highest efficiency. This higher efficiency of the GaAs control solar cell is due to higher open circuit voltage and better fill factor. This behavior can be interpreted, as shown in equation 1.7, by three factors. First the electron hole pair generation, parameter G, is higher due to good crystal quality of the homojunction grown GaAs solar cell. Thus the carriers are not trapped by material defects, complexes, and dislocations. Second the diffusion length of the minority carries in this homojunction

structure may be longer. Third the shunt resistance is higher. These factors may contribute individually or collectively to the higher open circuit voltage.

Regarding the normalized shunt resistance (R_p), it is very obvious form Table 5.1 that the GaAs control cells exhibits the highest value of R_p among the other solar cells. This may be due to high leakage current in the QD-based solar cells. Figure 5.4 illustrates a model for the different resistances associated with the solar cell structure as well as the ohmic contacts. Roughly, the values of normalized series resistance, R_s, and normalized shunt resistance R_p are obtained from the slope of the I-V curves shown in Figure 5.3 where R_s is obtained from the dV/dI slope near $V=V_{oc}$ and R_p is obtained from the dV/dI slope near $I= I_{sc}$. In these calculations the probe resistance is accounted for.

The ideality factor measures the quality and the degree of diffusion and recombination of the I-V characteristics of the pn diode. Unity ideality factor is desired because this indicates that the diffusion process is dominant. From Table 5.1 the ideality factor of the 6-stack InAs QD solar cell is the lowest with a value of 1.85. A defective material is subject to more recombination in which case, n will be closer to 2. The normalized saturation current, J_s, is also another important parameter to analyze. This parameter is a measure of leakage carriers in the pn junction. Mathematically, as I_s increase V_{oc} decrease, as shown in equation 1.7. From Table 5.1, the three-stack InAs QD solar cell has the highest J_s of 542nA/cm^2, which agrees with the significant drop in the V_{oc}. The I_s for the control cell and six-stack InAs solar cell are much lower 2.07 nA/cm^2 and 5.04 nA/cm^2, respectively, indicating higher material quality.

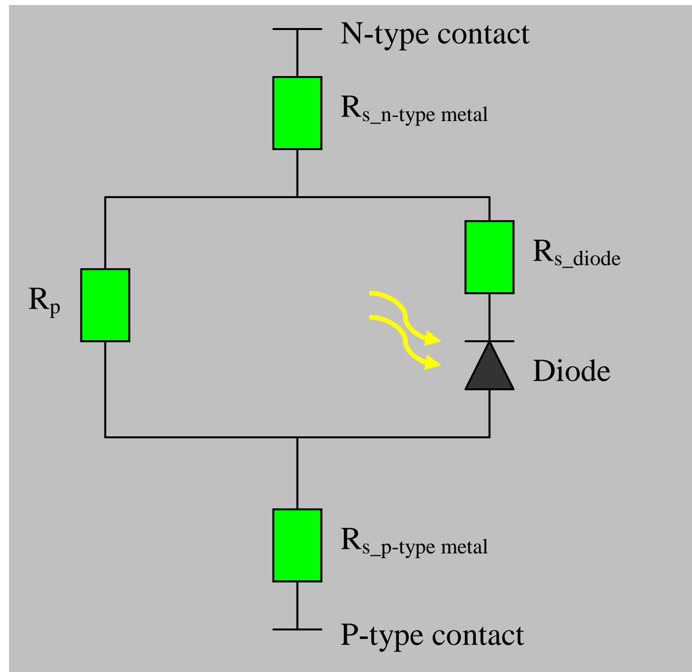

Figure 5.4 Equivalent circuit for resistance mechanisms involved in a solar cell.

5.2.2 Spectral response measurements of the ICP etched solar cells fabricated without silicon nitride sidewall passivation

The wavelength dependence of the photocurrent is measured to study the effect of placing the quantum dots in the i-region of the solar cells. The spectral responses for the three solar cells are presented in this section. Figure 5.5 illustrates the photocurrent measured for the 5x5 mm solar cells as a function of the wavelength.

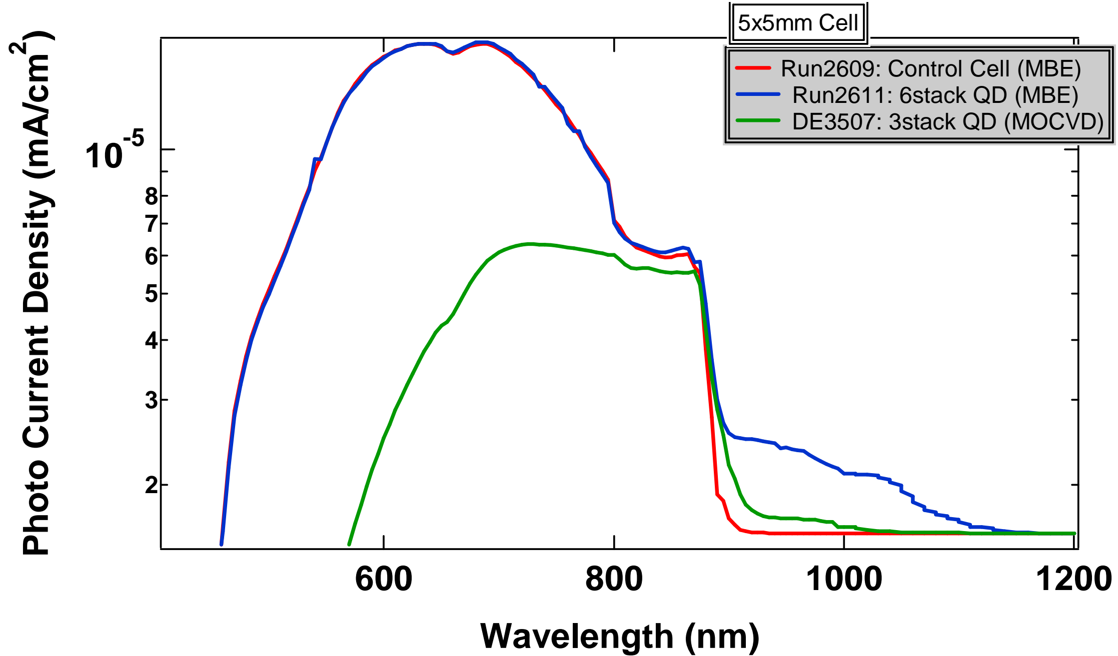

Figure 5.5 *The Spectral response for the 5x5mm control (red), 6-stack InAs QD(blue) and 3-stack InAs QD (green) solar cells fabricated by ICP etching and without sidewall passivation.*

As can be seen from Figure 5.5 the GaAs control sample, run 2609, and the MBE six-stack InAs QD solar cell, run 2611, have similar photocurrent density in the wavelengths less than 870 nm (GaAs band-edge wavelength). Both samples show higher photocurrent density than that of the MOCVD sample, run DE 3507. The difference in the photocurrent densities between MBE and MOCVD grown samples may be due to reduced crystal quality of the MOCVD sample or a low mobility emitter layer because the short wavelength response is so deteriorated. At wavelengths longer than the GaAs cutoff wavelength (870nm) both MBE six-stack and MOCVD three-stack solar cells demonstrate measurable photocurrent densities. This is strong evidence for the contribution of InAs QD photon absorption effect. In the contrary the GaAs control cell shows no photocurrent in this range. Also shown in Figure 5.5 the MBE six-stack sample, run 2611, has a higher photocurrent density than that of the MOCVD three-stack solar

cell in the InAs QD wavelength range (950-1200nm). This is due at least in part to more QD layers, as more layers are added to the structure the number of QD increases, with different QD sizes and densities. Unfortunately, as the number of the QD stacking layers increases there is a high possibility for degrading the material quality.

5.3 Characterization of the Wet Etched Mesa Solar Cells Fabricated with Silicon Nitride Sidewall Passivation

This section presents the devices made with the wet etched mesas and silicon nitride sidewall passivation. The purpose of implementing this technique is to improve the efficiency of the InAs QD solar cell. The MBE GaAs control cell and the InAs QD solar cell are processed using this method because they could potentially show better performance than the ICP method. It has been known that wet etching is a plane preferable etching technique while the ICP etching is not. This means by using wet etching crystal, dangling bonds are minimized and consequently the sidewall defects are reduced. In addition sidewall passivation will reduce leakage current in the device.

5.3.1 I-V measurements of the wet etched solar cells fabricated with silicon nitride sidewall passivation

This section presents the I-V measurements of the 5x5 mm solar cells grown by MBE. These solar cells are fabricated simultaneously under the same processing conditions, using wet etching with silicon nitride sidewall passivation. The I-V characteristics for the GaAs control and 6-stack InAs QD solar cells are presented in Figure 5.6. From this figure the open circuit voltage for the GaAs control and six stack

InAs QD solar cells are 0. 87V and 0.63V, respectively. While, the short circuit current density of both the GaAs and the InAs QD solar cells are 10.8mA/cm^2 and 11.3mA/cm^2, respectively.

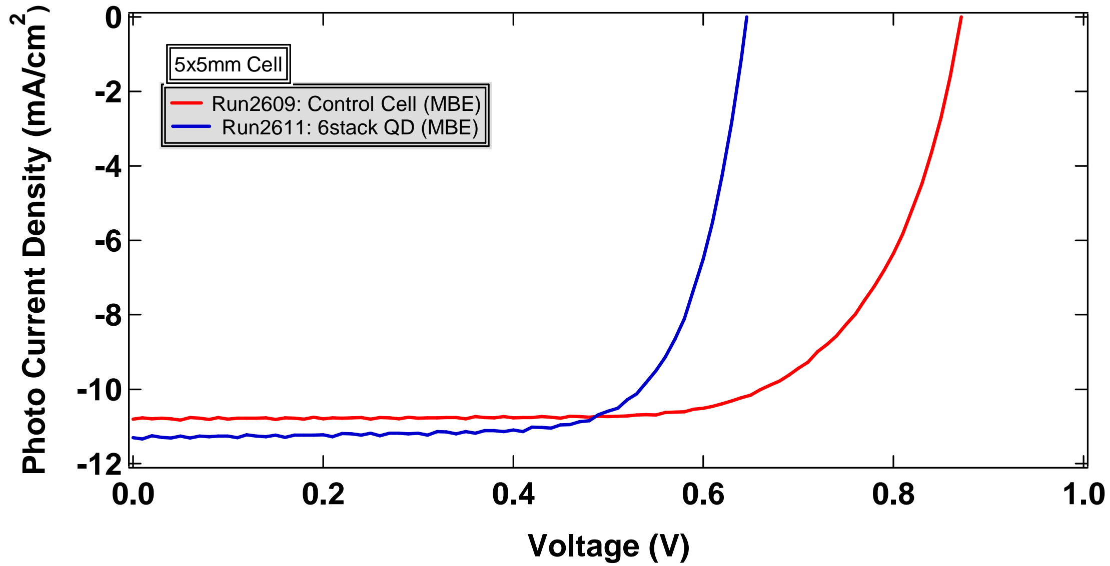

Figure 5.6 *The I-V characteristics for the 5x5mm GaAs control cell (red) and the 6-stack InAs QD(blue) solar cells fabricated by wet etching and passivated by silicon nitride.*

To study the performance of the solar cells fabricated using wet etching method the data measured from the I-V curves shown in Figure 5.6 are summarized in Table 5.2.

	Run2609: Control Cell	Run2611: 6-stack QD
Short Circuit Current Density (mA/cm^2):	10.8	11.3
Open Circuit Voltage (V):	0.87	0.63
Normalized P_{max} (mW/cm^2):	6.68	5.36
FF (%):	71.1	75.3
Efficiency (%):	8.35	6.70
Normalized Series Resistance ($\Omega.cm^2$):	0.658	0.910
Normalized Shunt Resistance ($k\Omega.cm^2$):	6.88	4.73
Ideality Factor (n):	1.97	1.79
Normalized Saturation Current (nA/cm^2):	0.922	4.32

Table 5.2 Summary for the MBE grown 5x5mm control and the 6-stack InAs QD solar cells fabricated by wet etching and passivated by silicon nitride.

This table shows that the six-stack InAs QD solar cell short circuit current density has increased from 10.6mA/cm^2 (see Table 5.1) to 11.3mA/cm^2. This increase is due to reduced dangling bonds and reduced leakage current as discussed above. Also the efficiencies of the six-stack InAs QD solar cell has slightly increased from 6.55% (see Table 5.1) to 6.70%. This increase is related to the increase in the short circuit current density, since the fill factor is nearly the same and V_{oc} is lower. The normalized series resistance, R_s, for both control cell and six-stack InAs QD solar cells are approximately the same for both processing techniques, see Table 5.1 and Table 5.2. On the other hand, the normalized shunt resistance, R_p, for both control cell and the six-stack solar cell has decreased using wet etching with sidewall passivation, which is a result of the slight increase in the I_{sc}. As for the ideality factor and the normalized saturation current for the

wet etched devices has decreased compared to the ICP etched devices. This can be related to the silicon nitride sidewall passivation, which reduces the sidewall dangling bonds and traps. This can be explained by reduced leakage current in the sidewall passivated samples.

5.3.2 Spectral Response Measurements of the Wet Etched Solar Cells Fabricated with Silicon Nitride Sidewall Passivation

Figure 5.7 illustrate the spectral responses of the GaAs control cell and six stack InAs QD solar cells fabricated by wet etching and passivated by silicon nitride. The photocurrent measured for the 5x5 mm solar cells is slightly higher than that presented in Figure 5.5. This result indicates that using different processing methods may improve some of the solar cell parameters.

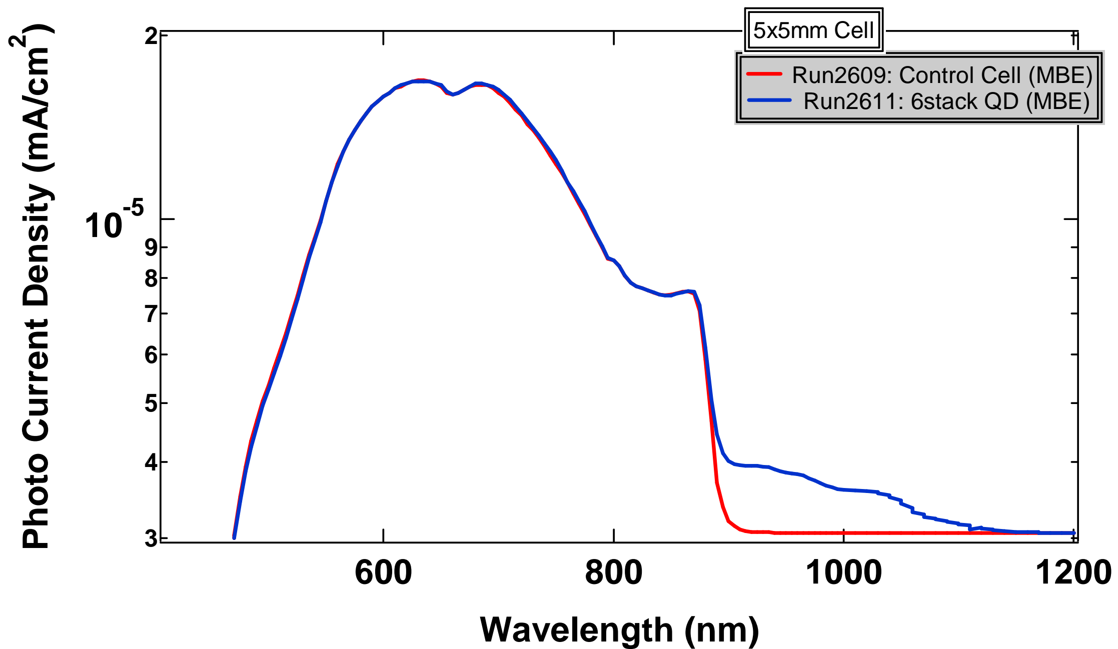

Figure 5.7 The Spectral response for the 5x5mm control (red) and 6-stack InAs QD (blue) solar cells fabricated by wet etching and passivated by silicon nitride.

As can be seen from Figure 5.7 the GaAs control sample, run 2609, and the MBE six stack InAs QD solar cell, run 2611 have similar photocurrent density in the wavelengths less than 870 nm. The six-stack InAs QD sample shows much higher photocurrent density beyond the GaAs bandgap wavelength (870 nm) related to the InAs QDs.

5.4 Scaling Effects of Six-Stack InAs QD Solar Cells

In this section the scaling effects for the 6-stack InAs QD solar cells will be discussed for the efficiency, short circuit current density, shunt and series resistance, and the other parameters. The scaling effect has been examined for samples fabricated by ICP and wet etching.

Figure 5.8 (a) and (b) show the I-V characteristics for the wafers processed by ICP and wet etching, respectively for 5x5mm, 3x3mm, and 2x2mm solar cell areas. Both techniques show an obvious increase the I_{sc}.

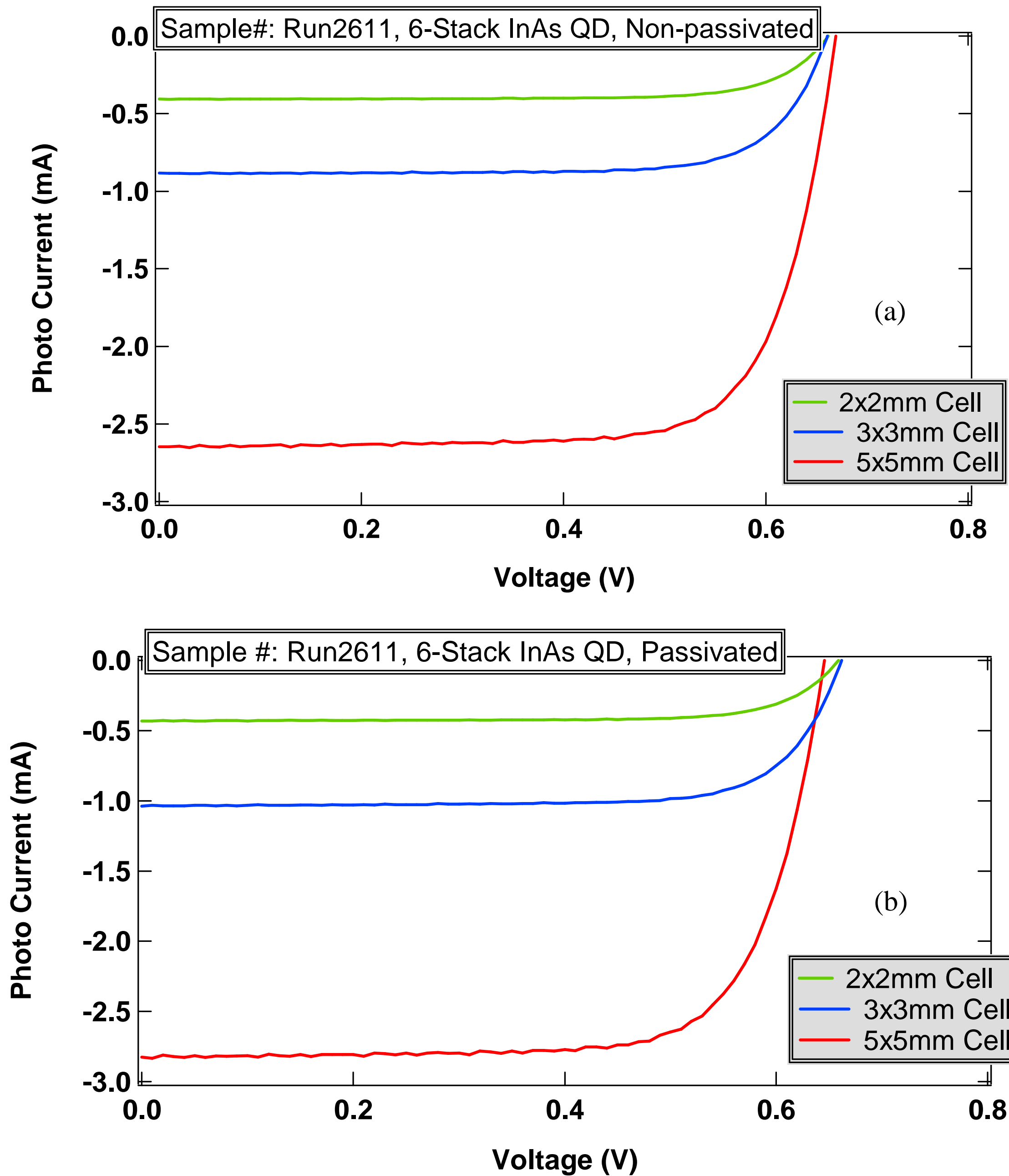

Figure 5.8 The I-V characteristics for the5x5mm (red), 3x3 mm (blue), and 2x2 mm (green) InAs six-stack QD solar cells. (a) ICP etched without silicon nitride passivation, (b) Wet etched with silicon nitride passivation. Both techniques show an obvious increase in the I_{sc}.

The biggest change occurs in the photocurrent, where the 5x5mm solar cell exhibits the highest photocurrent followed by the 3x3mm and 2x2mm solar cells.

Therefore, the total current of the solar cell is directly proportional to the effective area of the solar cell as shown in the current equations 1.3 and 1.5 presented in chapter 1.

On the other hand the open circuit voltage does not change with the solar cell area. This confirms that the open circuit voltage is a function of the technological parameters of the solar cell materials, such as doping, carrier diffusion length and recombination rates, see equation 1.7. As a result, the V_{oc} does not depend on the dimensions as given by equation 1.7 in chapter 1.

Table 5.3 summarizes the data obtained for the above two samples, processed by the ICP etching without Si_2N_3 passivation and the wet etched sample with Si_2N_3 passivation. From this data we see that the open circuit voltage and the conversion efficiency do not scale with the area, while the short circuit current increases with the area as expected. Note that Table 5.3 shows the short circuit current density. Figure 5.9 illustrates the short circuit current dependence on the area. Similar results are obtained for the GaAs control cell and the MOCVD three-stack InAs QD solar cell.

(a) ICP Etched (non-passivated) 6-stack InAs QD solar cells		**Area: 2x2mm**	**Area: 3x3mm**	**Area: 5x5mm**
Short Circuit Current Density (mA/cm^2):		10.2	9.86	10.6
Open Circuit Voltage (V):		0.66	0.66	0.67
Normalized P_{max} (mW/cm^2)		5.03	4.89	5.24
FF (%):		75.0	75.2	73.8
Efficiency (%):		6.28	6.11	6.55
Series Resistance	Normalized ($\Omega.cm^2$):	0.133	0.304	0.925
	Measured (Ω):	3.33	3.38	3.70
Shunt Resistance	Normalized ($k\Omega.cm^2$):	8.04	6.89	6.70
	Measured ($k\Omega$):	201	76.6	26.8
Ideality Factor (n):		1.52	1.54	1.85
Normalized Saturation Current (nA/cm^2):		0.645	0.707	5.04
(b) Wet Etched (passivated) 6-stack InAs QD solar cells				
Short Circuit Current Density (mA/cm^2):		10.8	11.6	11.3
Open Circuit Voltage (V):		0.65	0.66	0.63
Normalized P_{max} (mW/cm^2)		5.33	5.58	5.36
FF (%):		75.9	73.1	75.3
Efficiency (%):		6.66	6.98	6.70
Series Resistance	Normalized ($\Omega.cm^2$):	0.126	0.302	0.910
	Measured (Ω):	3.15	3.35	3.64
Shunt Resistance	Normalized ($k\Omega.cm^2$):	6.60	5.72	4.73
	Measured ($k\Omega$):	165	63.6	18.9
Ideality Factor (n):		1.43	1.46	1.79
Normalized Saturation Current (nA/cm^2):		0.308	0.387	4.32

Table 5.3 Summary for the 5x5mm, 3x3mm, and 2x2mm InAs six-stack QD solar cells. (a) ICP etched without silicon nitride passivation, (b) Wet etched with silicon nitride passivation.

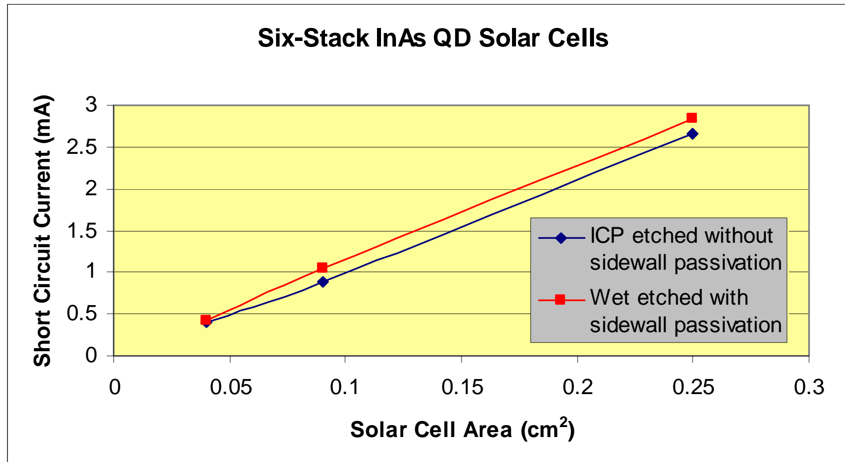

Figure 5.9 Six-stack InAs QD solar cell short circuit current versus solar cell area.

Table 5.3 also shows that the series resistance does not scale with the area. This can be explained by the simple model shown in Figure 5.10. In this model the series resistance consists of the contact resistance $R_{contact}$ and material resistance $R_{surface}$. The contact resistance increases when the area decreases due to the reduced width of the finger length. While, the material surface resistance decreases due to the reduction of the area exposed to light illumination. Therefore the total series resistance remains constant, as shown in Table 5.3.

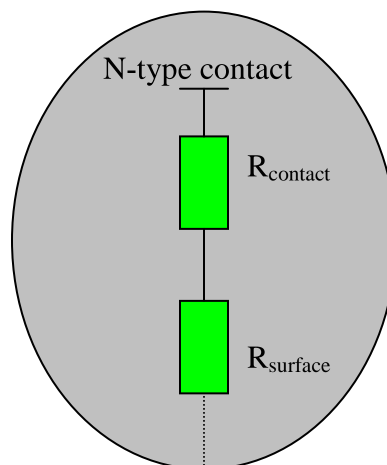

Figure 5.10 A simple model for the series resistance components when the solar cell device is scaled.

To explain this behavior we calculated the sheet resistance for the three areas using equation 5.1.

$$R_{sheet} = R_s \frac{L_{finger_length}}{L_{finger_gap}} \qquad (5.1)$$

Where R_s is the series resistance, L_{finger_length} is the length of the contact finger, and L_{finger_gap} is the gap length between contact fingers. These parameters are shown in Figure 5.11. Table 5.4 lists the L_{finger_length} and L_{finger_gap} for the different solar cell dimensions.

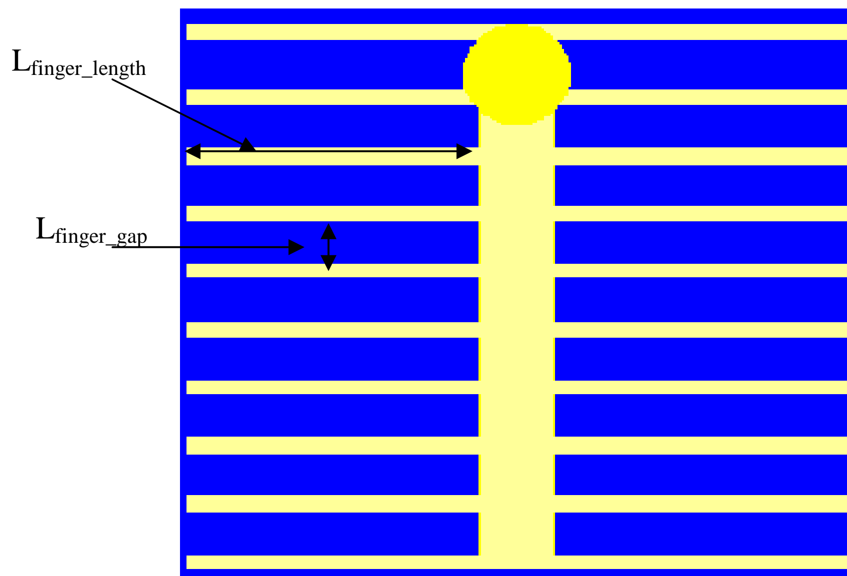

Figure 5.11 Solar cell illustration showing the finger length and finger gap.

	2x2mm Solar Cell	3x3mm Solar Cell	5x5mm Solar Cell
Finger length (cm):	0.0800	0.134	0.237
Finger gap (cm):	0.00800	0.0143	0.0285

Table 5.4 Finger length and gap for the 5x5mm, 3x3mm, and 2x2m solar cells.

Using the data from Table 5.4, the calculated values for the sheet resistances are shown in Table 5.5. Since all areas show the same values for the sheet resistance. The total series resistance should not change as discussed above.

	2x2mm Solar Cell	3x3mm Solar Cell	5x5mm Solar Cell
R_sheet ICP etched: Ω/□	32.3	31.7	30.8
R_sheet wet etched: Ω/□	31.5	31.4	30.3

Table 5.5 Sheet resistance values for the two six-stack InAs QD 5x5mm, 3x3mm, and 2x2m solar cells.

From Table 5.3 it can be seen that as the area of the solar cell gets smaller, the shunt resistance, the ideality factor, and the normalized saturation current values improve. This indicates that the 2x2mm solar cells exhibit the best values among the other cells pertaining to these three parameters. As the area decreases the defect density decreases due to material non-uniformity and as a result the carriers are not trapped. This shows that these three parameters are correlated.

CHAPTER 6 - Conclusion and Future Work

In this thesis, InAs QDs as intermediate band for solar cells (IBSC) is presented. It has been theoretically shown that IBSC can improve the conversion efficiency up to 63%. Therefore, the main focus of this thesis is to study the effect of inserting InAs quantum dots in the i-region of a GaAs based solar cell. In order to investigate InAs QDs as IBSC, three different samples were grown by MBE and MOCVD growth techniques.

The first sample is the MBE grown control solar cell, which does not have QDs. This sample is used as a reference sample to compare its results to the InAs QD solar cells. The second sample is the MBE grown InAs six-stack QD solar cell. The third sample is the MOCVD grown InAs three-stack QD solar cell.

The three samples are processed under the same conditions with two different processing methods, in order to compare the processing effects. The first set of samples were processed utilizing ICP etching without sidewall passivation while the second set were processed using wet etching with sidewall passivation.

From the I-V measurements the conversion efficiencies measured for the GaAs control cell, the MBE grown InAs six-stack solar cell, and the MOCVD grown InAs three-stack QD solar cell are 8.95%, 6.55%, and 1.33%, respectively. The lower efficiencies for the InAs QDs solar cells may be attributed to the strain effects between the InAs QDs in the intrinsic region and the overgrown layers. These strain effects may generate traps and non-radiative recombination centers for the electron hole pairs. The GaAs control cell lower efficiency is limited by the structure design, meaning pn homojunction. The MOCVD grown three-stack InAs QDs solar cells exhibits lower

efficiency, compared to the MBE grown six-stack InAs QDs due to lower QDs stacks and thus thinner i-region.

From the spectral response measurements InAs QD solar cells, grown by MBE or MOCVD, show photon absorption at wavelengths above GaAs wavelength to 1200 nm, indicating photon current contribution due to InAs QDs. Both the MBE grown samples, GaAs control cell and InAs six-stack solar cell, showed the same values for the photocurrent density below GaAs bandgap wavelength (870 nm). This indicates high quality material for the MBE grown samples.

Different processing techniques are used and showed that mesa structures with Si_2N_3 sidewall passivation have higher short circuit current. This may be due to lower leakage current and better sidewall crystal quality. This effect led to a slight increase in the QD solar cell efficiency fabricated using wet etching technique.

Scaling effects are studied by fabricating 5x5mm, 3x3mm, and 2x2mm solar cells. From the I-V measurements of these solar cells the short circuit current scales with the area while the series resistances do not scale with the area. This observation is explained by a simple model, which includes contact resistance and material resistance connected in series. Scaling down the device increases contact resistance while decreasing the material resistance. Both effects cancel each other, which keeps the total series resistance approximately constant. We also observed that the efficiencies and the open circuit voltage do not scale with the devices dimensions.

Future research work is needed to further investigate the IBSC model. New structure designs, with different bandgap materials, can be proposed to study the effect of

inserting InAs QDs as i-region in the solar cells structures [40]. In addition, new processing techniques may help improve the solar cell performance.

REFRENCES

[1] A. Luque, and A. Martí, “Increasing the efficiency of ideal solar cells by photon induced transitions at intermediate levels”, Phys. Rev. Lett. 78, 5014 (1997).

[2] J. Niemann, Keithley Instruments “Understanding solar cell physics: key to better testing methodology”, <http://archives.sensorsmag.com/articles/0504/57/main.shtml>, P.623, May (2004).

[3] C. Honsberg, “FAQ List for Solar Cells”.

[4] D.A. Neamen, “Basic principles: semiconductor physics and devices, McGraw Hill”, 3rd edition, 2003, P. 254-263.

[5] S.O. Kasap, “Optoelectronics and photonics principles and practices”, Prentice Hall Inc, First Ed., P 263.

[6] National Instruments Corporation, ‘Theory of I-V Characterization’, <http://zone.ni.com/devzone/cda/tut/p/id/7230#toc1>, September (2008).

[7] P. Bhattacharya, “Semiconductor optoelectronic devices”, New Jersey: Prentice Hall, 1994.

[8] B. Burnett, “The basic physics and design of III-V Multijunction solar cells”, National Renewable Energy Laboratory, <http://www.nrel.gov/ncpv/pdfs/11_20_dga_basics_9-13.pdf> ,summer 2002.

[9] Chemistry explained: foundations and applications, “Solar cells”, <http://www.chemistryexplained.com/Ru-Sp/Solar-Cells.html>, 2007.

[10] S.M. Sze, “Physics of semiconductor devices”, John Wiley & Sons, 2nd edition, 1981, P. 816.

[11] Lecture Handouts, UNM, ECE 570, fall 2006.

[12] D.J. Friedman, S.R. Kurtz, J.F. Geisz, “Analysis of the GaInP/GaAs/1-eV/Ge Cell and related structures for terrestrial concentrator application,” National Renewable Energy Laboratory, <http://www.nrel.gov/docs/fy02osti/32188.pdf>, 20-24 May 2002.

[13] M.A. Stan, D.J. Aiken, P.R. Sharps, N.S. Fatemi, F.A. Spadafora, J. Hills, H. Yoo, B. Clevenger, “27.5% Efficiency InGaP/InGaAs/Ge Advanced Triple Junction (ATJ) Space Solar Cells for High Volume Manufacturing”, Emcore, <http://www.emcore.com/assets/photovoltaics/29th_PVSC%20Stan.pdf >.

[14] K. C. Reinhardt, C. S. Mayberry, B. P. Lewis, T. L. Kreifels, “Multijunction solar cell iso-junction dark current study,” Photovoltaic Specialists Conference Record of the Twenty-Eight IEEE, Sept. 2000, P. 1118 – 1121.

[15] Chu, C. “GaInP2 and GaAs solar cells grown on Si substrate”, Photovoltaic Specialists Conference Record of the Twenty-Eight IEEE, Sept. 2000, P. 1250 – 1252.

[16] “Solar cell structures”, U.S. Department of Energy, <http://www1.eere.energy.gov/solar/printable_versions/solar_cell_structures.html >, 23 December 2005.

[17] R. R. King, D. C. Law, K. M. Edmondson, C. M. Fetzer, G. S. Kinsey, H. Yoon, R. A. Sherif, and N. H. Karam, “40% efficient metamorphic GaInP/GaInAs/Ge multijunction solar cells”, APPL. Phys. Lett. 90, 183516 (2007).

[18] A. Luque, A. Martí, P. Wahnón, L. Cuadra, C. Tablero, C. Stanley, A. McKee, D. Zhou, R. Könenkamp, R. Bayón, A. Belaidi, J. Alonso5, J. Ruiz5, J. Fernández, P.

Palacios, N. López, “Progress toward the practical implementation of the intermediate band solar cells”, IEEE, 1190-1193, (2002).

[19] W. Shockley, and H. J. Queisser, “ Detailed balance limit of efficiency of p-n junction solar cell”, J. Appl. Phys. 32, 510 (1961).

[20] C. M. Wolfe , N. Holonyak , G. E. Stillman, "Physical properties of semiconductors”, 1989, P.121.

[21] http://www-opto.e-technik.uni-ulm.de/lehre/cs/DOS-DIM.jpg.

[22] K. W. J. Barnham and G. Duggan, “A new approach to high-efficiency multi-band-gap solar cells”, J. Appl. Phys. 67, 3490 (1990).

[23] M. Paxman, J. Nelson, B. Braun, J. Connolly, and K. W. J. Barnham, “Modeling the spectral response of the quantum well solar cell”, J. Appl. Phys. 74, 614 (1993).

[24] U. Aeberhard, R. Morf, “Microscopic modeling of quantum well solar cells”, Springer Vienna, 10.1007/978-3-211-72861-1_56, (2007).

[25] V. Aroutiounian, S. Petrosyan, and A. Khachatryan, “Quantum dot solar cells”, J. Appl. Phys. 89, 4, February (2001).

[26] M. Bonn, FOM-Institute AMOLF, “Hot carriers in quntum dots for solar cells”, ppt.

[27] R.D. Schaller, M. Sykora, J.M. Pitryga, and V.I. Klimov, “Seven excitons at the cost one: Redefining the limits for conversion efficiency of photons into charge carriers”, Nano lett. 6, 424 (2006).

[28] S. Suraprapapich, S. Thainoi, S. Kanjanachuchai, S. Panyakeow, “Quantum dot integration in heterostructure solar cells”, Semiconductor Device Research

Laboratory, Department of Electrical Engineering, Faculty of Engineering, Chulalongkorn University.

[29] S. Sinharoy, C.W. King, S.G. Bailey, and R.P. Raffaelle, "InAs quantum dot deployment for enhanced InGaAs space solar cells", 31st IEEE PVSC, 94 (2005).

[30] S. M. Hubbard, R. Raffaelle, R. Robinson, C. Bailey, D. Wilt, D. Wolford, W. Maurer, and S. Bailey, "Growth and Characterization of InAs Quantum Dot Enhanced Photovoltaic Devices", Mater. Res. Soc. Symp. Proc. Vol. 1017 (2007).

[31] A. Marti, L. Cuadra and A. Luque; "Partial filling of a quantum dot intermediate band solar cells", IEEE trans. On Elec. Dev. Vol 48, No. 10, 2394 (2001).

[32] R.B. Laghumavarapu, Ph. D dissertation, University of New Mexico

[33] S. Ghosh, B. Kochman, J. Singh, P. Bhattacharya, "Conduction band offset in InAs/GaAs self organized quantum dots measured by deep level transient spectroscope", Appl. Phys. Lett. 76, 2571 (2000).

[34] A. Marti, "Intermediate band solar cells", JRC ISPRA Nov. (2005)

[35] F. Rinaldi, "Basics of Molecular Beam Epitaxy (MBE)", http://www-opto.e-technik.uni-ulm.de/forschung/jahresbericht/2002/ar2002_fr.pdf.

[36] A. Stintz, G. T. Liu, A. L. Gray, R. Spillers, S. M. Delgado, and K. J. Malloy. "Characterization of InAs quantum dots in strained InxGa1-xAs quantum wells", J. Vac. Sci. Technol. B 18 (3), 1496-1501 (May-Jun 2000).

[37] www.materials.web.psi.ch/Research/ThinFilms/Methods/Images/MOCVD_sc.jpg

[38] A. A. El-Emawy, S. Birudavolu, P.S. Wong, Y.–B. Jiang, H. Xu, S. Huang, and D.L. Huffaker, "Formation Trends in Quantum Dot Growth using Metalorganic Chemical Vapor Deposition" J. Appl. Phys. 93, p. 3529-3534 (March 15, 2003).

[39] A. Luque and A. Martı´, C. Stanley, N. Lo´pez and L. Cuadra, D. Zhou and J. L. Pearson, A. McKee, "General equivalent circuit for intermediate band devices: Potentials,currents and electroluminescence", Appl. Phys. Lett.96, 1 (2004).

[40] R.B. Laghumavarapu, M. El-Emawy, N. Nuntawong, A. Moscho, L.F. Lester and D.L. Huffaker, "Improved device performance of InAs/GaAs QD solar cells with GaP strain compensation", Appl. Phys. Lett. 91, 243115 (2007).